

AD-A252 883



EOS



Electro-Optical Sciences, Inc.
1 Bridge Street
Irvington-on-Hudson, NY 10533
Tel: 914/591-3783
Fax: 914/591-3785

19 June 1992

DRAFT FINAL REPORT
(CDRL A002)

Laser Doppler Experiments

N00014-90-C-0214

SDTIC
ELECTE
JUL 16 1992
S A D

Authored by:

Theodore Shultz
Douglas Brenner
Marek Elbaum
Michael Greenebaum
George Lind

Electro-Optical Sciences, Inc.
1 Bridge Street
Irvington, NY 10533

Prepared for:

Robert Mongeon
Office of Naval Research
495 Summer Street
Boston, MA 02210

This document has been approved
for public release and sale; its
distribution is unlimited.

EOS/FR-0214

DEFENSE TECHNICAL INFORMATION CENTER



9216739

92 6 24 086

CONTENTS

		<u>Page</u>
1.0	INTRODUCTION	1
1.1	PRINCIPAL ACCOMPLISHMENTS	1
2.0	EXPERIMENT GOALS AND APPROACH	3
2.1	DIRECT-DETECTION DOPPLER INTERFEROMETRY AND TEXTURE IMAGING CONCEPTS	3
2.2	TARGET KINEMATICS AT ISTEf	4
2.3	STEP-WISE APPROACH TO DATA COLLECTION	5
3.0	OPTICAL DESIGN AND IMPLEMENTATION	8
3.1	DESIGN OF THE INTERFEROMETER AND TRANSFER OPTICS	8
3.2	BEAM EXPANDER DESIGN	9
3.3	HARDWARE SUMMARY	10
4.0	ELECTRONIC DATA-COLLECTION INTERFACE	11
5.0	CALIBRATION ISSUES	13
6.0	TEXTURE IMAGING PERFORMANCE ANALYSIS	14
6.1	RADIOMETRIC ANALYSIS	14
6.2	SPECKLE CONTRAST ANALYSIS	15
7.0	SUMMARY AND RECOMMENDATIONS	19
	REFERENCES	20
	APPENDIX: RADIOMETRIC CALCULATIONS	61

Statement A per telecon Mathew White
 ONR/Code 126
 Arlington, VA 22217-5000

NWW 7/15/92

Accession For	
NTIS CRA&I	<input checked="" type="checkbox"/>
DTIC TAB	<input type="checkbox"/>
Unannounced	<input type="checkbox"/>
Justification	<input type="checkbox"/>
By _____	
Distribution / _____	
Availability Codes	
Dist	Avail and/or Special
A-1	:

FIGURES

<u>Figure</u>	<u>Page</u>
1. Doppler direct detection methods.	22
2. Image texture method.	23
3. Delta-2 target details.	24
4. Kinematic implications.	25
5. Data quantity (kinematic implications).	26
6. EOS step-by-step approach to data collection (PDR).	27
7. Experiment 1: No tracking, 2-m spot.	28
8. Optical Schematic.	29
9. Experiment 2: No tracking, 5-m spot.	30
10. Hardware for Experiment 1.	31
11. Detector packages.	32
12. Field lens parameters.	33
13. Beam splitters.	34
14. Air-spaced wedge etalon.	35
15. Receiver optics for autodyne.	36
16. Transmission fringe sensitivity to incidence angle.	37
17. Transmission fringe sensitivity to field of view.	38
18. Transfer optics--field-of-view considerations.	39
19. Transfer optics--parameters.	40
20. Beam expander concept.	41
21. Beam expander for autodyne experiments.	42
22. Electronics--block diagram.	43

FIGURES (Concluded)

45

<u>Figure</u>	<u>Page</u>
23. Calibration.	44
24. Comparative field-of-view chart.	45
25. Target board calibration.	46
26. Calibration board on gantry.	47
27. Signal photon counts: plume and hard body--2-m beam.	48
28. Signal photon counts: plume and hard body--5-m beam.	49
29. Background photon counts.	50
30. Lidar "signal to noise ratio".	51
31. Expression for speckle contrast.	52
32. Turbulence effects--spherical waves, $\lambda=0.532 \mu\text{m}$.	53
33. Predictions for very low turbulence.	54
34. Turbulence effects--spherical waves, $\lambda=1.064 \mu\text{m}$.	55
35. Contrast modulation due to beam steering: approximate one-dimensional analytical formulation.	56
36. Contrast modulation due to beam steering: gaussian model, $\sigma=1.5 \text{ m}$, $\Delta_{\text{res}}=0.42 \text{ m}$.	57
37. Contrast modulation due to beam steering: gaussian model, $\sigma=2.5 \text{ m}$, $\Delta_{\text{res}}=0.42 \text{ m}$.	58
A-1. Radiometric analysis of signal photocounts per resel.	62
A-2. Atmospheric parameters vs slant range.	63
A-3. Radiometric analysis of background photocounts per resel.	64
A-4. Parameters employed for radiometric analysis	65

TABLES

<u>Table</u>	<u>Page</u>
I. Target & system parameters.	59
II. Background.	60

1.0 INTRODUCTION

This document constitutes the Final Report on Contract N00014-90-C-0214/P00001, "Relative Merits of Innovative Imaging Sensor Systems," and covers the period 18 January 1991 through 12 April 1992. The purpose of the work was to conduct research and assist efforts in ground-based optical identification and tracking at the Innovative Science and Technology Experimental Facility (ISTEF) in Florida. The technology areas covered included signal processing, the collection of target signature data, and proof-of-concept field demonstrations of sensor systems. A major portion of the work centered on the design of a laser Doppler field experiment which would be suitable for deployment at ISTEf, a site which is uniquely well suited for obtaining signature data relevant to the rocket lift-off episode. Extensive documentation of interim results is contained in earlier reports which were delivered to the sponsor on three occasions: at the Preliminary Design Review (PDR) on 15 October 1991 (Ref. 1); at an intermediate briefing on 9 January 1992 (Ref. 2), and at the Critical Design Review (CDR) on 14 February 1992 (Ref. 3). In the present report, we discuss the methods used in the underlying analysis and recapitulate the key results and recommendations obtained.

Section 2 discusses the goals and the approach recommended by EOS, Inc. for fielding data collection experiments in support of laser Doppler imaging. As detailed in that Section, a two-stage/four-experiment approach is recommended for achieving these goals. Considerations of optical design and implementation are treated in Section 3. The electronic and data-collection aspects of the experiment are treated in Section 4. Section 5 deals with calibration issues and Section 6 discusses the Texture Imaging technique. Section 7 contains our summary and recommendations.

1.1 Principal Accomplishments

The initial period of the program was concerned with assessing the ISTEf site facilities. These included the seeded, doubled Nd:YAG laser which was physically located at CREOL, and the Contraves 0.5-m telescope, located at TTC. These two major pieces of equipment are vital for the experimental program leading to proof-of-concept demonstrations of autodyne, Doppler and texture image tracking techniques.

During the course of characterizing this equipment and determining what was necessary for integration at ISTEf, a sequential experiment plan was developed. This four stage program provides an early opportunity to collect active target returns to verify photometric calculations and equipment performance. The next stage would produce calibrated measurements of target reflectivity and demonstrate texture imaging. The third stage would incorporate interferometric measurement of Doppler signatures to evaluate autodyne potential and the final stage would attempt closed-loop tracking. The plan allows for early active data collection, with the less complex early stages designed for maximum likelihood of success; the plan should integrate well with the development of advanced instrumentation necessary for Doppler data collection, which is necessarily more complex.

The work has emphasized the mechanical, optical and electronic design of the apparatus to date. The Contraves mount was fitted with new coude mirrors for the YAG laser; the beam expander was removed and a new window installed; and a new lens designed and installed in the receiver to allow the use of an existing mechanism for focusing. A new back plane for the Contraves has been designed to accommodate sensors for 0.53 μm and 1.06 μm , CCD imaging and a fiber optic feed to the interferometer. This back plane is currently under construction.

To accelerate the implementation of the interferometer, a fixed, ruggedized version was designed and ordered. Field lenses for the detectors and fiber optics were designed and tested and the fibers themselves procured. Isolation filters for the CREOL laser power monitors were designed, procured and delivered to CREOL. In turn, CREOL delivered detectors for the laser returns to EOS. These were tested and were found to require mechanical and electrical modification for compatibility. Beam splitters and mounts to separate the received signals by wavelength and function are on hand.

Much of the data recording capability resides at ISTEf and will be put into operation during the preliminary laser measurement phase. EOS has developed the software to use a LeCroy multichannel digitizer to record the detector outputs. Designs for synchronization of cameras and laser have been developed and are awaiting implementation.

2.0 EXPERIMENT GOALS AND APPROACH

The objectives of the experiments discussed in this report are as follows:

- To obtain Doppler data on the plumes of in-flight rockets by laser interferometric means--the first time this will be done.
- To obtain calibrated data on the plume reflectance during rocket flight--also the first time this will have been accomplished.
- To demonstrate the feasibility of the texture imaging concept--another first.
- To identify the trailing edge of the rocket in an image containing elements both of the plume and of the hard body. This would be done either by means of texture-imaging or by combining the angle-angle image information with Doppler discrimination data.

2.1 Direct-Detection Doppler Interferometry and Texture Imaging Concepts

The key concept which these experiments seek to validate in the field is that one can obtain supplementary information useful for tracking by discriminating laser returns scattered by the rocket plume from returns scattered by the hard body through the use of suitable apparatus added on to a conventional telescope. In particular, one can employ discrimination based on the Doppler spectrum. Alternatively (or additionally), one may discriminate between the image textures characteristic of rockets and of their plumes, as described below.

The first method--Doppler spectra via direct detection--is illustrated in the upper part of Figure 1. Consider a generic rocket, traveling to the left, illuminated by a laser spot whose diameter is comparable to that of the rocket. If the spot reflects solely from the rocket body (spot #1 in the figure), a narrow Doppler-shifted return is expected, as schematically illustrated by the inset figure at the top left. If the laser spot is intercepted by the plume alone (spot #3 in the figure), the Doppler return will be centered at a different frequency, because the mean of the component of the line-of-sight velocity will differ from that of the rocket, and the spectrum will be spread out because of variations in the line-of-sight velocity components of different particles in the illuminated portion of the plume. This characteristic of the plume Doppler spectrum is illustrated in the inset figure at the top right. The interface between the hard body and the plume will be contained in the scatter from a spot such as that labeled #2 in the figure. The interface will not be resolvable from the image alone, but can be located through the use of the auxiliary information which is sought in the experiments under discussion.

The conventional way to obtain the Doppler information from laser scatter return signals would be to use heterodyne interferometry, a method best suited to infrared wavelengths. Coherent detection methods are more difficult to implement at visible

wavelengths, whereas rocket bodies do not reflect very well in the infrared. The laser Doppler techniques of interest to us employ direct detection instead. In the lower portion of Figure 1, two such methods are shown. The first is the autodyne method shown on the left, which yields relative Doppler shifts, i.e., there is no indication of the sign of the shift. The second technique is the interferometric method, which is easier to implement at the present state of technology. In the interferometric approach, a multibeam Fizeau interferometer (MBFI) is employed along with anamorphic optics to generate the Doppler signatures, and one can distinguish positive from negative Doppler shifts within the free spectral range (FSR) of the instrument. For a typical design considered, $FSR = 20$ to 30 GHz.

The other novel technique whose requirements we analyze is the image texture method, illustrated schematically in Figure 2. In the figure, we consider a detector in the form of a linear imaging array of diffraction-limited pixels. Let the characteristic Doppler spread of the plume be denoted by Δv_p and denote the Doppler width associated with the hard body by Δv (which includes the finite coherence of the laser, the effective resolution of the interferometer, etc.). Then, by employing an integration time T_2 such that $1/\Delta v_p < T_2 < 1/\Delta v$ (e.g., T_2 on the order of 100 ns), one can distinguish between hard body scattering and plume scattering by the differently fluctuating natures of the two types of returns: the plume image will tend to have a smoother distribution of intensity vs pixel position than will the highly speckled image expected from the hard body.

2.2 Target Kinematics at ISTEf

The ISTEf site in Florida is uniquely well suited for tracking rocket bodies and their plumes during the period immediately following ignition and liftoff. For purposes of designing an experiment to test laser radar tracking concepts at ISTEf, we consider the Delta-2 rocket, whose essential mechanical features are indicated in Figure 3. The essentially cylindrical rocket body is 30 to 40 meters long; it is powered by rocket motors whose outer periphery is contained in a circle 4.5 m in diameter. The plume properties during the lift-off episode visible from ISTEf are governed by the propellant characteristics listed in the figure; scattering contributions are to be expected from the exhaust plumes of both types of rocket, i.e., liquid- (LOX/RP-1) and solid-fueled (14% Al).

Based on consideration of the rocket kinematics, one can estimate the quantity of data to be expected during the course of a lift-off experiment. For the Delta rocket, with a thrust $T = 860$ klbs and weight $W = 484$ klbs, the thrust length will be approximately 40 m and the target acceleration will be $a = (T/W - 1)g = 7.78 \text{ ms}^{-2}$, so that the target velocity v_T (m/s) will increase with altitude h (m) as $v_T = (2ha)^{1/2}$. We consider an experiment in which the laser illumination forms a spot aimed at a fixed altitude and the target flies through the beam. The projected laser spot will have a beam diameter D_B (n); in order to "paint" the entire rocket body with such spots at a pulse repetition frequency PRF (Hz) with an overlap factor OL between adjacent spots, D_B must satisfy the following relationship:

$$D_B = (2ha)^{1/2} (1+OL)/PRF.$$

Taking PRF = 10 Hz, the spot diameter projected by the fixed laser beam should lie between the two limiting curves indicated on Figure 4 in order to cover the target more-or-less uniformly during the data collection episode. The two limiting curves assume either (1) no overlap between successive beam positions, or (2) 50% overlap between successive spots. As noted on the figure, the spot size required (from kinematic considerations alone) becomes larger than the width of the booster for altitudes above 60 m or so.

The length of time that the target remains in the field of view in such an experiment can now be calculated. Hence, as Figure 5 indicates, the number of data frames associated with the rocket body as it passes through the fixed laser beam will be on the order of 10 to 30 (depending on beam altitude), if one assumes that the data rate is governed by the 10-Hz PRF. Thus, an initial experiment predicated upon having the rocket pass through a fixed laser beam should be capable of yielding statistically significant data, provided that the rocket does pass through the beam.

2.3 Step-wise Approach to Data Collection

From the results shown in Figures 4 and 5, the constraints imposed by requiring the laser to have a fixed pointing direction become clear. To obtain data on rocket bodies and plumes at altitudes above 60 m or so, it will be necessary to go beyond such a first-phase experiment. Of course, once tracking of the target during the experiment is required, more complex hardware will be needed.

EOS, Inc. has given serious consideration to the nature of the information which it is reasonable to expect can be obtained with and without tracking. Figure 6--originally presented at the PDR (Ref. 1) and repeated at the CDR--summarizes the two-stage, four-experiment step-wise approach for data collection which we have developed. The two experiments during Stage 1 are limited to the lift-off episode and do not obtain Doppler signature data and do not require tracking the target. Experiments 3 and 4, both aimed at obtaining Doppler signature data, would have to take place during Stage 2, since the target would need to be tracked. In Experiment 3, manual tracking would suffice, but automatic means of tracking would be highly desirable for Experiment 4.

2.3.1 Experiment 1: No Tracking, 2-m Spot

The data collection plan for Experiment 1 calls for obtaining calibrated returns from the laser-illuminated hard body and target at two wavelengths, one in the visible (doubled Nd:YAG at 0.532 μm) and one in the near-infrared (Nd:YAG at 1.063 μm). The experiment plan also calls for demonstrating the ability to perform spatially resolved texture imaging at the shorter wavelength (in the laboratory, in preparation for Experiment 2).

To implement Experiment 1 (Figure 7), one would employ a laser illuminator pointing at a fixed location, and no tracking would be required (although manual tracking would be valuable, of course, as would real-time range data). The optical design would yield a spot diameter of approximately 2 m at the target, without the need for beam-forming optics. The target vehicle would move through the fixed beam while the receiver gathers the scattered return. The receiver design calls for a 50-cm collecting aperture, with the received signals split into three paths (Figure 8 (a)). The first path leads to an infrared "photon bucket" detector such as an avalanche photodiode (APD). The second path leads to an intensified charge-coupled detector (ICCD) camera, gated synchronously to the laser pulse to achieve background rejection, especially self-luminous and ambient-scattered radiation from the plume. The third path leads to a "photon bucket" (e.g., an APD) for the visible channel at 0.532 μm .

2.3.2 Experiment 2: No Tracking, 5-m Spot

The data collection plan for Experiment 2 is designed to obtain laser returns from complex targets, including glints, etc. Emphasis will be placed on expanding the calibrated target cross-section data base at the same wavelengths as in Experiment 1. Another major goal is to obtain spatially resolved texture images of the target at 0.532 μm . (As an alternative, should it be judged that sufficient target cross-section data is available following Experiment 1, Doppler interferometric measurements could be commenced during Experiment 2.)

To implement Experiment 2 (Figure 9), modifications to the optics would be desirable, so as to increase the beam size while matching the detector field of view to the beam (Figure 8(c)). Beam-forming optics would allow the beam size to increase to 5 m at in the infrared. (Should beam forming optics not become available in a timely manner, beam expanders would be omitted, and the MBFI would be used with the same green laser line as in Experiment 1.) As was the case for Experiment 1, Experiment 2 could be performed with the laser beam fixed in position, but it would be highly desirable to be able to track the target manually. For this purpose, a pre-programmed trajectory would be required, along with real-time range updates.

Finally, as indicated in Figure 8(b), should the signal levels expected at the photodetectors be sufficiently high, one would replace the ADP at 0.532 μm (in the third path in Figure 8 (a)) by an optical fiber connecting to the MBFI followed by a gated camera.

2.3.3 Experiment 3

Experiment 3 calls for obtaining Doppler data, from both the hard body and the plume, to evaluate the potential of autodyne tracking techniques. To implement Experiment 3, the green APD would be replaced by an optical fiber receiver with a field lens whose numerical aperture is matched to that of the fiber. The other end of the fiber will be located in the laboratory and its output will feed the MBFI.

The results of Experiments 1 and 2 will be used to determine the signal levels that can be expected, so that the optimum split between the CCD camera and the MBFI can be selected and the appropriate beam splitter installed in the receiver. Beam splitters with a range of splitting ratios from 10 percent to 50 percent are on hand.

As described in Section 3.1, there is a set of optimum parameters for the interferometer. Inasmuch as the interferometer is located near the exit pupil of the receiver telescope, the telescope field-of-view will be restricted. For full utilization of all green photons in the interferometer, the optimum field-of-view would be 0.2 milliradian, which corresponds to a 2-meter spot at a target 10-km distant. This would necessitate adjustment of the beamforming optics from the 5-meter spot in Experiment 2. Depending on the results of the laser characterization tests and the consequent beam expander design, it is planned to maintain the IR beam as in Experiment 2.

2.3.4 Experiment 4

At present, ISTEf does not employ closed-loop target tracking. For this reason, during Experiments 1, 2 and 3, the illumination beam is initially fixed and directed above the target, pre-launch, and the target is allowed to move through the beam. Tracking will be done manually after the missile and plume have moved through the beam.

It is expected that, by the time Experiment 4 is implemented, some form of closed-loop tracking will be exercised. It is intended to build into the tracking routine a programmed variable bias so that the illuminating beam will be "painted" over the target. The specific details depend on what track algorithm is employed. This will be developed during the course of closed-loop track implementation. If the closed-loop track can follow the target with a substantial increase in the target range, it may be necessary to exercise other variables. These include: a sliding range gate; programmed beamforming optics to maintain beam size; and programmed focus control. Inputs for controlling these variables can be derived from predictive range estimation and updated by real-time range measurement using the laser pulse and a timer. It is intended to investigate this capability during the manual track phase of Experiments 1 and 2.

3.0 OPTICAL DESIGN AND IMPLEMENTATION

The optical design for Experiments 1 and 2 was performed in sufficient detail to draw up a hardware list for presentation at the CDR (Figure 10). Several key components were ordered and received, as listed in Figure 11. As received, the avalanche photodiodes (APD's) were not suitable and they have had to be modified. The optical parameters of the field lenses for the various detectors are listed in Figure 12. The beam splitters, which were designed for a 22.5-deg incidence angle, have been tested. The measured values for the splitting ratios are compared with the design values in Figure 13.

3.1 Design of the Interferometer and Transfer Optics

The MBFI design calls for an optically contacted air-spaced wedge etalon to ensure reliability (Figure 14). RFQ's were issued to four potential vendors, eliciting two responses (from Continental and from TecOptics). Continental's bid was accepted. Their 12-week delivery time (measured from 18 February) should allow testing, assembly and shipment in time for availability at ISTEf in July.

A key parameter in designing the transfer optics linking the MBFI to the receiver aperture is the field of view required for experiments at ISTEf. As indicated in Figure 15, the maximum angular deviation from the nominal line of sight is magnified by the aperture ratio in a matched-f/# design. The reason for concern is indicated by consideration of the data shown in Figures 16 and 17. The calculations summarized in these figures assumed the nominal parameters for the MBFI shown on the upper left: Free spectral range FSR = 15 GHz at wavelength $\lambda = 0.532 \mu\text{m}$; equal 93% reflectances (essentially lossless) at the two surfaces which are inclined at a wedge angle $\alpha = 16 \mu\text{rad}$.

The abscissa in Figure 16 gives the nominal incidence angle θ_0 with respect to the normal to the first reflecting surface;¹ the calculations assumed a field-of-view subtending a cone of half-angle $\theta_s = 1 \text{ mrad}$ (i.e., FOV = 2 mrad). The triangle-bearing dashed curve in Figure 16 plots the variation in peak transmission with incidence angle (right-hand scale), assuming that fringe intensity contributions associated with collimated light originating from different directions add incoherently; a 9-point quadrature rule was used. When the line of sight deviates by more than $\approx 1 \text{ mrad}$ from the optimal value ($\theta_0 \approx -0.5 \text{ mrad}$), the peak intensity drops two-fold.

The solid curve in Figure 16 indicates the location of the average-intensity peak, while the short-dashed curves indicate the locations of the half-intensity points (relative

¹ A negative sign indicates incidence from the side of the normal opposite the apex of the wedge. The calculation was done for fringes observed just past the second reflecting surface. For fringe observation in other planes, the optimal incidence angle changes, but the curves in Figure 16 retain their shape.

to the peak intensity for a given θ_0). Fringe location is expressed in milli-orders (m-order) on the left-hand ordinate scale, i.e., in units of $FSR/1000$,² since $FSR = 15$ GHz, a shift of 10 m-order corresponds to a frequency shift of 150 MHz. The curves in Figure 16 indicate that a field lens designed for a 1-mrad field of view should keep the FWHM below ≈ 300 MHz, and that a well-aligned MBFI can locate peaks to an accuracy ≤ 100 MHz.

The choice of mirror reflectances for the interferometer plates and the tolerance to be placed on the field of view have been determined by means of the calculations such as the one summarized in Figure 17. For this calculation, the reflectances of the plates are 94% and the spacing between the plates has been increased so that FSR is now 12 GHz (as indicated in the figure heading). The solid curve in Figure 17 indicates the dependence of the FWHM (full width between half-transmission points near the peak intensity--left-hand ordinate scale) upon the field of view, i.e., as a function of the half-angle of the cone defining the field of view ($FOV = 2\theta_s$). The dashed curve plots the field-of-view dependence of the maximum transmission of the interferometer, averaged over the field of view (to be read from the right-hand scale). With this design, a maximum (averaged) transmission of 80% or better requires a smaller field of view ($2\theta_s \approx 1.5$ mrad instead of 2 mrad). The associated FWHM would then be greater (≈ 500 MHz) despite the decreased free spectral range.

Figure 18 shows the top-level considerations in designing transfer optics employing a fiber optic light guide. The focal length is related to the fiber diameter by the considerations shown in Figure 19. In our design, we first characterized available fiber optics by their numerical apertures at the input and output ends. Then we selected a suitable combination of fiber diameter and numerical aperture, selected a field lens to go with it. The next step was to design the collimator.

3.2 Beam Expander Design

As indicated above (Sec. 2.3.2), it is desirable for a properly designed beam expander to be available in time for Experiment 2. This experiment is designed to acquire signature data at two wavelengths, one in the infrared--with a 5-m beam--and the other in the visible--with a smaller beam diameter needed for the Doppler measurements. A beam expander is desirable to maintain control of the optical paths independently at the two wavelengths. The optical design must ensure proper optical correction at each wavelength, while maintaining collinearity of the two beams (Figure 20). The philosophy underlying the design of the beam expander is summarized in Figure 21.

² The "zero" reference is the expected position of the peak at normal incidence; it is the peak position only in the (Fabry-Perot) limit that the wedge angle tends to zero.

3.3 Hardware Summary

The following salient points were made at the Critical Design Review, 14 February 1992:

- The design and testing of hardware for Experiment 1 is on schedule.
- The optical design for the autodyne and Doppler interferometric measurements achieves an instrument performance which is within a factor of 2 of the theoretical optimum based on first principles.
- Resolution of remaining design uncertainties are not expected to cause delay in data collection.
- Definitive measurements of the laser energy distribution are needed in order to ensure photometric integrity of the Doppler data.
- Authorization from ONR to proceed with procurement was sought and obtained at the CDR.

4.0 ELECTRONIC DATA-COLLECTION INTERFACE

Figure 22 constitutes a block diagram of the control and signal circuitry associated with the telescope and the apparatus to be mounted on it for Experiment 1.

Since several organizations shall be participating in the experiment, it is essential that the responsibilities of each be spelled out. The break-out of responsibilities proposed at the CDR is as follows:

(1) EOS, Inc. would be responsible for the following:

- Data acquisition and control computer and its associated hardware
- CAMAC
- Avalanche photodiodes and associated DC power supplies and amplifiers.
- Signal compatibility--from the laser trigger to the CAMAC, from the time gate generator to the Xybion camera, and from the laser power supply to the CAMAC.
- Subject to Air Force approval, EOS would employ the Cohu camera (owned by the USAF) for monitoring the beam quality.

(2) NRC/ISTEF would be responsible for the following:

- Provide the Xybion and tracking cameras. Using synchronization signals derived from the Xybion camera, gen lock the tracking and beam monitoring camera.
- Synchronize the laser triggering to the Xybion camera:
 - Obtain a frame counter (a 30 Hz signal indicating the start of a frame) from the Xybion camera or any other device that uses the camera's sync signals as input.
 - Divide the frame counter rate by 3 to obtain the desired laser pulse repetition frequency of 10 Hz.
 - Send the 10-Hz signal to the laser to initiate charging of the laser lamps.
 - Sense the laser's end-of-charge signal.
 - Send the "fire" command.

The required pulse durations and amplitudes are listed in the laser manual or can be obtained directly from the manufacturer (Continuum).

- Make available the Tektronix Model 602 digitizing signal analyzer.
- Record all video signals with IRIG B

- Supply the IRIG B signal to EOS
- Supply cabling between remote locations including:
 - 2 RG-58 cables with BNC's at least 200 ft long
 - Cables from the sensors to the recording locations.
 - Sync cable to the laser.
- Provide means (via relay or otherwise) of starting the laser immediately prior to rocket ignition.
- Supply video monitors where needed.
- Supply intercoms and/or other communication equipment as needed.
- Supply 100 VAC power for EOS equipment; two 15-amp outlets should suffice.

(3) CREOL would be responsible for the following hardware:

- Nd:YAG laser (as specified elsewhere).
- Laser power monitors, incorporating filters supplied by EOS.

5.0 CALIBRATION ISSUES

Issues relating to radiometric calibration for field experiments at ISTEf were treated in Refs. 1 and 2 and are summarized here. Briefly, calibration is essential (1) to ensure the colinearity of the optical systems for the visible ($0.53 \mu\text{m}$) and infrared ($1.06 \mu\text{m}$) beams, as well as (2) to check for significant departures of the illumination patterns from their nominal far-field shapes.

The method suggested for ensuring colinearity is to employ ancillary sensors in both the visible and infrared regions which observe a target calibration board containing reference beacons. Each camera would be aligned with the center beacon; spot locations would be measured with respect to a reticle. Additional beacons could be used to estimate r_0 , so as to quantify optically significant atmospheric turbulence conditions. If done carefully, the calibration procedure also may be able to estimate the atmospheric transmission along the path. (See Figure 23, from Ref. 1).

The fields of view of the various optical devices considered for use in Experiment 1 are summarized in Figure 24 (from Ref. 2); the fields of view of the Contraves and the Xybion camera are shown as centered on a Delta-2 rocket body, viewed from a range of 10 km. Full field for the Xybion corresponds to 16 mm along the diagonal; the corresponding diagonal for the ITT camera is 18 mm. The dashed-line rectangles indicate the maximum fields (along the vertical and horizontal directions) when imaging the target with one of three lenses on the ITT camera: 10" f/12 ($4.7 \text{ mr} \times 3.5 \text{ mr}$), 12" f/12 ($3.9 \text{ mr} \times 3.0 \text{ mr}$), and 12" f/15 ($3.1 \text{ mr} \times 2.4 \text{ mr}$).

Figure 25 (from Ref. 2) describes one method of system calibration based on the imaging of a reference beacon. Conceptually, one would locate the center of the field of view relative to the beacon image, as indicated in the figure for the example of the ITT camera employing the 12" f/15 lens.

The target reflectance in the green region should be on the order of 0.3/sr, measured without filters, at night. As indicated in Figure 26 (from Ref. 1), one could place a painted target board on the rocket gantry and calibrate immediately prior to lift-off. The placement of a target board on the rocket gantry may not be practical. An alternative site, a lighthouse at nearly the same range, with a similar azimuth angle, has been identified. This site might be suitable for calibration once the reflectance characteristics have been measured.

6.0 TEXTURE IMAGING PERFORMANCE ANALYSIS

An introduction to the image texture method was presented in Section 2 (see Figure 2). The purpose of a field experiment for texture imaging is to demonstrate the applicability of the technique for obtaining bounds on the plume-induced Doppler shifts and for locating the trailing edge of the rocket. EOS, Inc. has analyzed the feasibility of performing a demonstration experiment on texture imaging at ISTEf. The analysis consists of the following: (a) signal-to-noise (radiometric) calculations, (b) estimation of the effects of clear air turbulence on the image texture (leading to an expression for speckle contrast), and (c) performance predictions for the conditions likely to apply at ISTEf.

6.1 Radiometric Analysis

In the measurement of target reflectance, a key quantity is the signal-to-noise ratio of the measurement. We may model the total number n_{total} of photocounts received in terms of an overall system constant C_{syst} , along with the beam-target overlap function ψ (which includes the effects of jitter), the two-way atmospheric attenuation τ_a , the effective target reflectance ρ and an additive term n_b (representing background and electronic noise) as follows:

$$n_{total} = C_{syst} \psi \tau_a \rho + n_b$$

Reflectance estimates are based on mean values, i.e.,

$$\rho = \langle n_{total} \rangle / C_{syst} \langle \psi \rangle \langle \tau_a \rangle.$$

However, since photocounts fluctuate, we must also consider the variance of the total number of photocounts:

$$\frac{\text{var}(n_{total})}{[\langle n_{total} \rangle - \langle n_b \rangle]^2} = \frac{\text{var}(\psi)}{\langle \psi \rangle^2} + \frac{\text{var}(\tau_a)}{\langle \tau_a \rangle^2} + \frac{1}{SNR_{bkgd}} \quad (1)$$

where

$$SNR_{bkgd} = [\langle n_{total} \rangle - \langle n_b \rangle]^2 / \text{var}(n_b) \quad (2)$$

Table I indicates the target and system parameters employed for radiometric calculations by EOS, as well as the parameters employed in independent calculations by P. Gatt of CREOL and by F. Tart of W.J. Shafer & Associates. Similarly, Table II lists the assumptions made concerning the plume background radiometry by EOS and

by the same two other parties. Justification for the assumptions made by EOS has been documented in Ref. 4. (See also Refs. 5 and .) An Appendix to this report contains the equations used for the radiometric calculations. Here, it suffices to present the results of these calculations.

Figure 27 shows the total number of signal photons collected as a function of range (upper two curves) which are associated with the plume and with the hard body, respectively. (As noted in Table I, we assume that the plume reflectance is twice that of the hard body.) For these calculations, the beam diameter, which is 2 m at a range of 10 km (as in Experiment 1), scales linearly with range. When the total number of photons collected is divided by the number of resolution cells in the image of the plume, the lower (solid) curve is obtained, representing the mean number of photocounts per resel in the plume, for slant ranges appropriate to launches likely to be visible from ISTEf in Experiment 1; one expects to have on the order of 100 to 1000 signal photocounts per resel at all realistic ranges.

When the calculation is repeated for the 5-m beam diameter appropriate to Experiment 2, Figure 28 is obtained. (The line types have the same significance as in Figure 27.) At ranges less than 17 km, one still expects in excess of 100 signal photocounts per resel on the plume.

Turning now to the photocount level expected from the plume background, we obtain the results shown in Figure 29 for two different assumptions. In case 1, the receiver footprint at 10 km is 3 m, as would be appropriate to Experiment 1. Case 2, which assumes a 6-m footprint, corresponds to Experiment 2. Since the plume fills the field of view, and since atmospheric turbulence is expected to limit the achievable resolution for this viewing geometry, both cases produce the same number of background photocounts per *turbulence-limited* resolution cell. For this first-cut calculation, a constant value of 5 cm is assumed for the coherence diameter r_o , independent of range, and the area of the associated resolution cell is $\frac{\pi}{4} \left(\frac{\lambda R}{r_o} \right)^2$. (Further discussion of atmospheric turbulence is deferred until Sec. 6.2.)

Next, we combine the results shown in the preceding two figures to obtain the "naive" lidar signal-to-noise ratio for observing the plume signal against the plume background noise-- SNR_{bkgd} of Eq. (2) (i.e., ignoring all other sources of noise in Eq. (1))--as shown in Figure 30. Even for case 2 (i.e., Experiment 2), the background-noise limit to the per-resel signal to noise ratio exceeds 10:1 at all ranges, and exceeds 100:1 at ranges below 18 km.

6.2 Speckle Contrast Analysis

We showed many years ago (Refs. 7-8) that one may employ a linear-systems approach to calculation of the speckle contrast of laser scatter from a rough target in the presence of atmospheric turbulence. As indicated in Figure 31, we consider a transmitter aperture at plane X_1 which illuminates a target at plane X_o . The scattered radiation is observed by the receiver at plane X'_1 (co-located with the transmitter)

which images the target onto the image plane X_2 . At the image plane, the complex amplitude associated with the k^{th} scatterer, denoted by $U_k(x_2)$ is calculable as the triple convolution indicated on the figure. The notation is such that $B(x_0 - x_1)$ represents the "raw" beam amplitude at the target (in the absence of turbulence), $G_A(\bullet)$ represents a Green's function associated with the turbulence, $h(\bullet)$ denotes the transfer function of the receiving telescope, and the target reflectance function possesses a time-dependent argument which associates the complex amplitude with the k^{th} scatterer. The intensity measured by the detector is calculated from the squared modulus of U_k , summed over all scatterers in the region of overlap between the beam footprint and the receiver field of view. We make a delta-correlation (localization) approximation such as is conventional for analysis of speckles in scattering from rough surfaces. The final result of a triple-product covariance analysis is that the speckle contrast will not be much perturbed by the presence of turbulence, provided that the coherence diameter r_o is smaller than the (turbulence-limited) resolution cell.

We follow the example of David Fried (Ref. 9) in representing the influence of clear-air turbulence on the optical system by the coherence diameter, r_o , which is defined on the basis of the wave structure function $D_w(r)$, where r denotes transverse separation across the wave-front; this function represents the mean-square deviation of the (complex) wavefront from the value it would have in the absence of turbulence. In the Kolmogorov inertial subrange of turbulence (well-developed turbulence), the wave structure function scales with the coherence diameter according to the 5/3-law:

$$D_w(r) = 6.44 (r/r_o)^{5/3}$$

where r_o is a function of the wavelength and of the altitude- and range-dependent micrometeorology. For homogeneous turbulence, the range- and wavelength-dependences can be factored out; for more complicated situations, numerical integration is required. For purposes of estimating r_o , we started with the turbulence profile suggested by Greenwood (Ref. 10) (which was based on data at the ARPA Maui Optical Station (AMOS), Ref. 11) and adapted it to the near-sea-level site geometry at ISTEFL. For a slant range $R = 10$ km between points located at heights $h = 5$ to 10 m above MSL, the model predicts the following range of values for r_o :

$$\begin{aligned} r_o &= 5 \text{ to } 16 \text{ mm at } 0.532 \text{ } \mu\text{m} \\ &= 12 \text{ to } 36 \text{ mm at } 1.064 \text{ } \mu\text{m} \end{aligned}$$

Such values are consistent with data obtained near ground level in carefully controlled field measurements conducted by RADCO over grassy, more-or-less level terrain near Verona, NY (Ref. 12). Altitude dependence is assumed to follow a -1.3 power law, i.e., turbulence strength scales according to $(h+h_o)^{-1.3}$, with $h_o = 0.01$ m.³

³ To be precise, we took $C_n^2 = [.0043 \exp(-h/4000.) + 22.(h+.01)^{-1.3}] \times 10^{-14} [\text{m}^{-2/3}]$.

For present purposes, we estimate the turbulence-limited effective resolution of the receiver telescope, Δ_{res} , from the approximate relation:

$$\Delta_{res} \approx \lambda R / r_o$$

where λ is the wavelength and R is the slant range (mks units).

Figure 32 displays the results of applying the turbulence model to computing the coherence diameter and the turbulence-limited receiver resolution (both expressed in mm) at $\lambda=0.532 \mu\text{m}$, over horizontal ranges ≤ 10 km, between points at altitude 5, 10 and 30 m above sea level. It is evident from the plots that the coherence diameter is likely to be significantly smaller than Δ_{res} at all realistic ranges available at ISTEf.

It is important to take the turbulence levels properly into account; if one were to employ uncharacteristically small values for the Kolmogorov structure parameter near ground level, one would obtain results such as illustrated in Figure 33, where the same power scaling with $(h+.01[\text{m}])^{-1.3}$ is assumed, but C_n^2 at $h=10$ m has the smaller value indicated on the figure.

At $\lambda = 1.064 \mu\text{m}$, the expected coherence diameter and resolution cell sizes are as shown in Figure 34--for same the realistic turbulence model as in Figure 32. Although at this longer wavelength the coherence diameter is greater and the turbulence-limited resolution cell is smaller, it is still expected that $r_o < \Delta_{res}$ at ranges exceeding ≈ 5 km.

A related issue in an image texture experiment is the amount of contrast modulation that one expects on account of the beam steering induced by atmospheric turbulence. An approximate analytical model for the contrast modulation induced by such beam steering is the following: Suppose that the beam profile is modeled as a one-dimensional Gaussian (in variable x), and that the profile is displaced a distance $\pm\delta$. The average of such a profile over a region of width Δ is calculable in terms of the error function $\text{erf}(\cdot)$, so that the contrast modulation takes the analytic form indicated in Figure 35, for the special case that the averaging region equals the turbulence-limited resolution cell size. The contrast modulation due to beam steering calculated in this manner is plotted in Figures 36 and 37 for Gaussian beams with $2\text{-}\sigma$ widths of 3 m and 5 m, respectively, for the case indicated by the solid line in Figure 32 (i.e., a 10-km path 5 m above MSL) at a wavelength of $0.532 \mu\text{m}$. The local-averaged contrast modulation amounts to $\pm 14\%$ for the 3-m beam and $\pm 8.4\%$ for the 5-m beam.

Our analysis of speckle contrast in the presence of turbulence seems to be borne out by experimental work done at the Oregon Graduate Center (Refs. 13-14) which indicates that speckle contrast will be near unity, independent of turbulence, when turbulence is strong ($\sigma_1^2 = \sigma_{Rytov}^2 \gg 0.1$), as well as when turbulence is very weak ($\sigma_1^2 \leq 0.1$). In the intermediate regime of turbulence, Fante's formulation (Ref. 15) predicts that the normalized intensity variance follows the asymptotic trend:

$$\sigma_1^2 = 1 + 0.99 / (\sigma_1^2)^{2/5}$$

Our conclusion is that for stationary Lambertian targets (such as hard rocket bodies in the visible), the speckle contrast--including turbulence effect--will be ≥ 1 , but for fast-moving plume particles, the speckle contrast will be $\ll 1$. These fundamental assertions underlie the validity of the texture image discrimination concept and they should be capable of being tested at ISTEf.

7.0 CONCLUSIONS

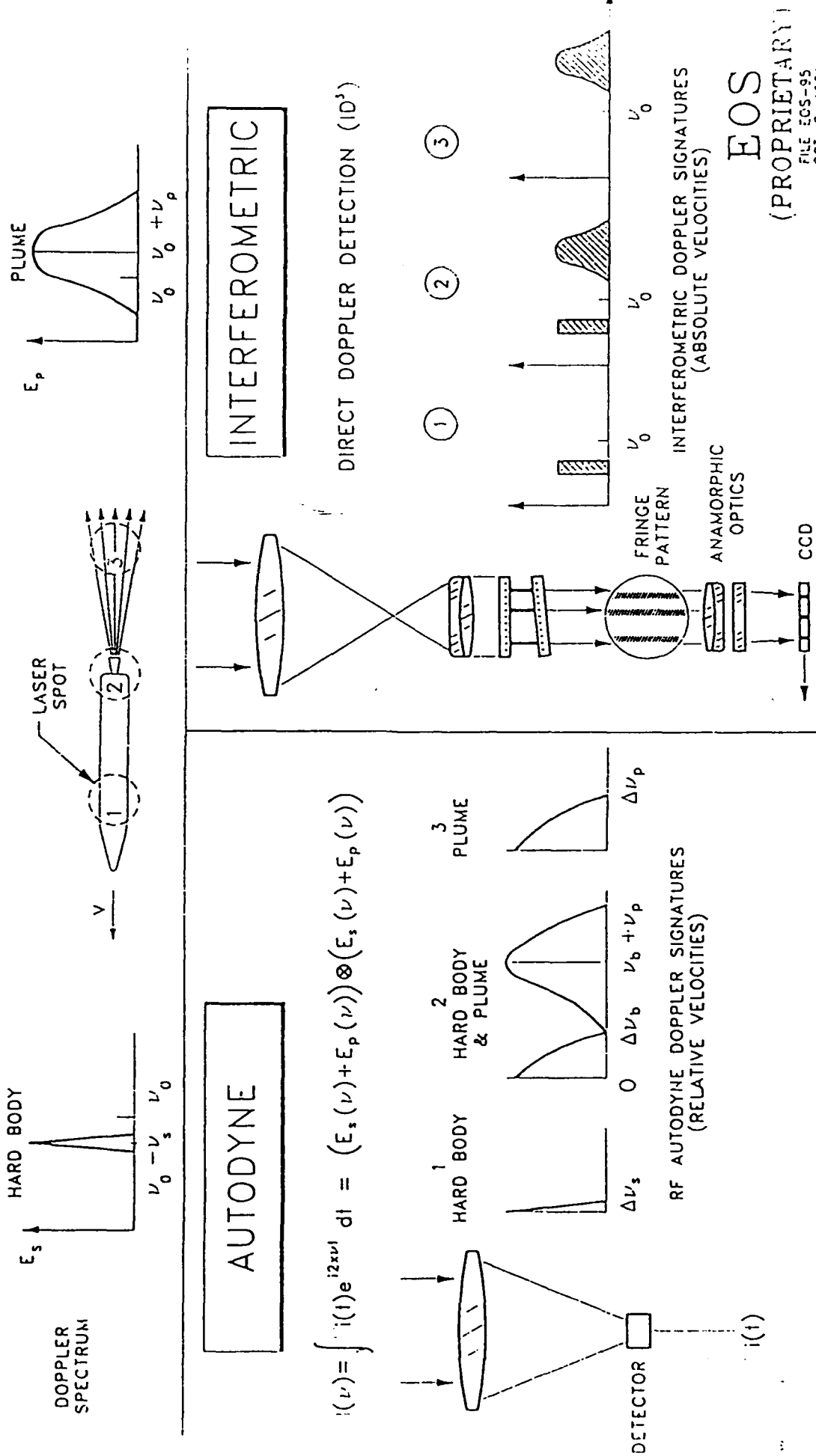
From the analyses, design studies and experiment plans accomplished so far, there appear to be no major obstacles to conducting the experiments, as designed, at ISTEf. Data from these experiments, after reduction and analysis, will allow several important goals to be achieved. First, the estimates of expected target returns either would be verified or would need to be corrected. Secondly, there will now be a data base for subsequent high-altitude active tracking experiments. If similar targets are used for balloon experiments, for example, there will be a set of real numbers to compare against. Thirdly, it will be possible to assess the feasibility of using autodyne techniques for robust active tracking in the presence of plumes. By scaling the data, one can predict signal levels, Doppler bandwidths, temporal stability and dynamic range and thereby study hardware options and algorithms to determine whether autodyne tracking can be implemented. Fourthly, it is expected that texture imaging as a result of Doppler bandwidth differences will be demonstrated. These results will generate concepts for new active discrimination and tracking techniques.

Finally, if Experiment 4 can be implemented in future efforts, it will serve as a test bed to evaluate interferometric direct detection algorithms against real images in determining position estimate accuracy and bias.

REFERENCES

1. Shultz, T., Elbaum, M., Brenner, D. and Greenebaum, M., "Laser Doppler Experiment," Preliminary Design Review, EOS, Inc., Irvington, NY, 15 October 1991.
2. Shultz, T., Brenner, D., and Elbaum, M., "Laser Doppler Experiment," ONR-PR-92-1, EOS, Inc., Irvington, NY, 9 January 1992.
3. Shultz, T., Elbaum, M., Brenner, D. and Greenebaum, M., "Laser Doppler Experiments: Critical Design Review," CDRL92-1.ONR, EOS, Inc., Irvington, NY, 14 February 1992.
4. Shultz, T., private communications to F. Tart, et al., February 1992.
5. Shultz, T., "Visit to CREOL, Orlando, 12-17 February 1991," Summary Report 2-91, Electro-Optical Sciences, Inc., Irvington, NY, February 1991.
6. Shultz, T., "Integration of 0.5-m Contraves with ISTEf Experimental Program," Summary Report 4-91, Electro-Optical Sciences, Inc., Irvington, NY, 19 April 1991.
7. King, M., Greenebaum, M. and Elbaum, M., "Influence of the Atmosphere on Laser-Produced Speckle Patterns," Digest of Papers Presented at the 1974 International Optical Computing Conference, April 9-11, 1974, Zurich, Switzerland, Institute of Electrical and Electronics Engineers, Inc., New York, N.Y., IEEE Catalog No. 74 CH0862-3C, pp. 64-68.
8. Greenebaum, M., "The Residual Effects of Atmospheric Turbulence on a Class of Holographic Imaging and Correlography Systems," Digest of Technical Papers, Topical Meeting on Optical Propagation Through Turbulence, July 9-11 1974, University of Colorado, Boulder, CO, Paper Th A6 (Available from Optical Society of America, Washington, D.C.).
9. Fried, D.L. and Mevers, G.E., "Evaluation of r_0 for Propagation Down Through the Atmosphere," Applied Optics, Vol. 13, pp. 2620-2622 (1974); Errata: Vol. 14, p. 2567 (1975).
10. Greenwood, D.P., "Bandwidth Specification for Adaptive Optics Systems," J. Opt. Soc. Amer., Vol. 67, pp. 390-393 (1977).
11. Miller, M, Zieske, P. and Hanson, D., "Characterization of Atmospheric Turbulence," *Proceedings of the SPIE/SPSE Technical Symposium East on Imaging Through the Atmosphere*, Vol. 75, paper 75-05 (1975)--cited in Ref. 10.

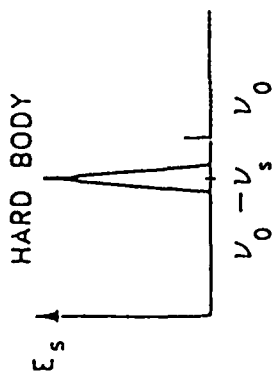
- 12 Greenwood, D. P. and Tarazano, D. O., "A Proposed Form for the Atmospheric Microtemperature Spatial Spectrum in the Input Range," RADC-TR-74-19, Rome Air Development Center, Griffiss AFB, NY, February 1974.
13. Pincus, P.A., Fossey, M.E., Holmes, J.F. and Kerr, J.R., "Speckle Propagation through Turbulence: Experimental," J. Opt. Soc. Amer., Vol. 68, pp. 760-762 (1978).
14. Holmes, J.F., Lee, M.H. and Kerr, J.R., "Effect of the Log-Amplitude Covariance Function on the Statistics of Speckle Propagation through the Turbulent Atmosphere," J. Opt. Soc. Amer., Vol. 70, pp. 355-360 (1980).
15. Fante, R., "Electromagnetic Beam Propagation in Turbulent Media," Proc. IEEE, Vol. 63, No. 12, pp. 1669-1692 (1975).



$$i(\nu) = \int i(t) e^{i2\pi\nu t} dt = (E_s(\nu) + E_p(\nu)) \otimes (E_s(\nu) + E_p(\nu))$$

Figure 1. Doppler direct detection methods.

DOPPLER SPECTRUM



$$1/\Delta\nu_p < T_2 < 1/\Delta\nu_s$$

$$T_2 \approx 1 \mu\text{sec}$$

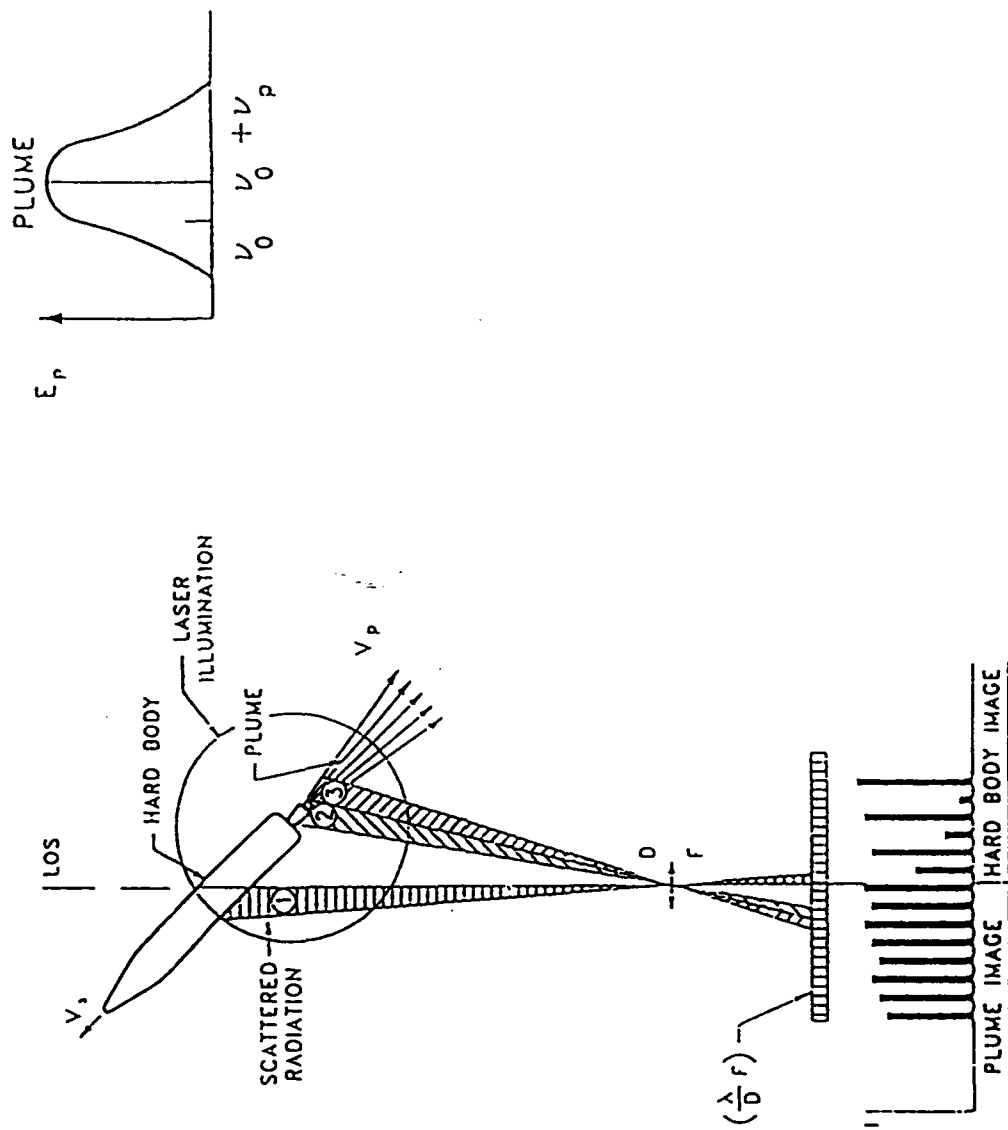
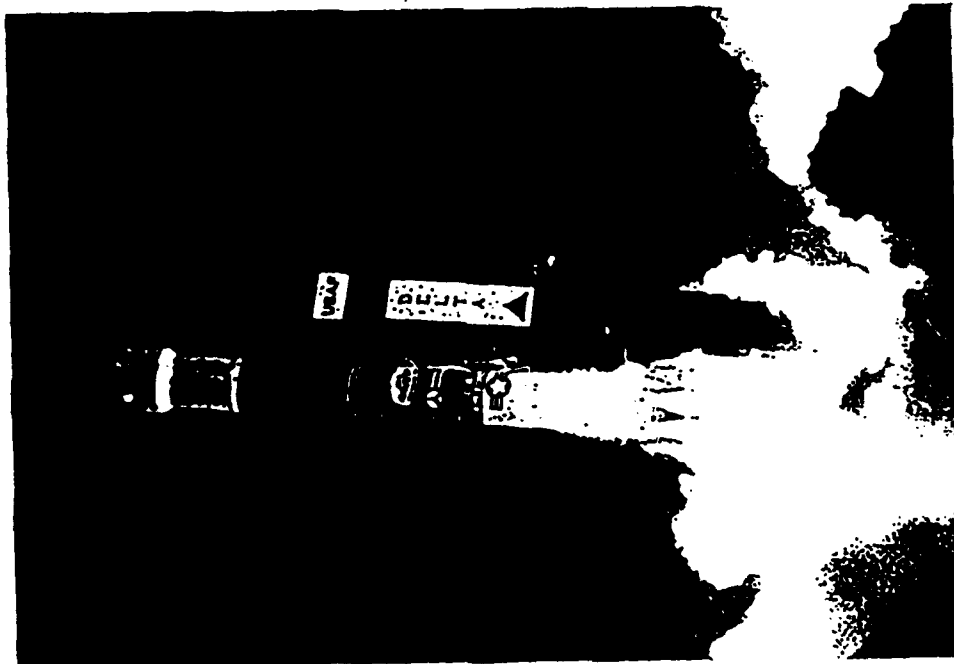


Figure 2. Image texture method.

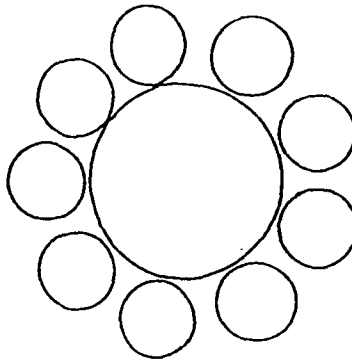


McDonnell Douglas Delta 2 lifts off at Cape Canaveral carrying an Air Force Rockwell Navstar/Global Positioning System satellite into orbit.

BODY LENGTH 30 OR 40 METERS

DELTA-2 TAIL-ON VIEW

- 9 SOLID MOTORS
- 3.3' DIA.
- 90 Klbs Thrust each
- 6 Fire @ Launch
- 3 FIRE @ 60 SEC
- 14% ALUMINUM
- 2 VERSIONS - 36' OR 44' LENGTH



← 45m →

- 1 LIQUID RS 27
- 8' DIA.
- LOX/RP-1
- 230 Klbs Thrust
- TYC
- BURSTS LIFTOFF TO 265 SEC.

Figure 3. Delta-2 target details.

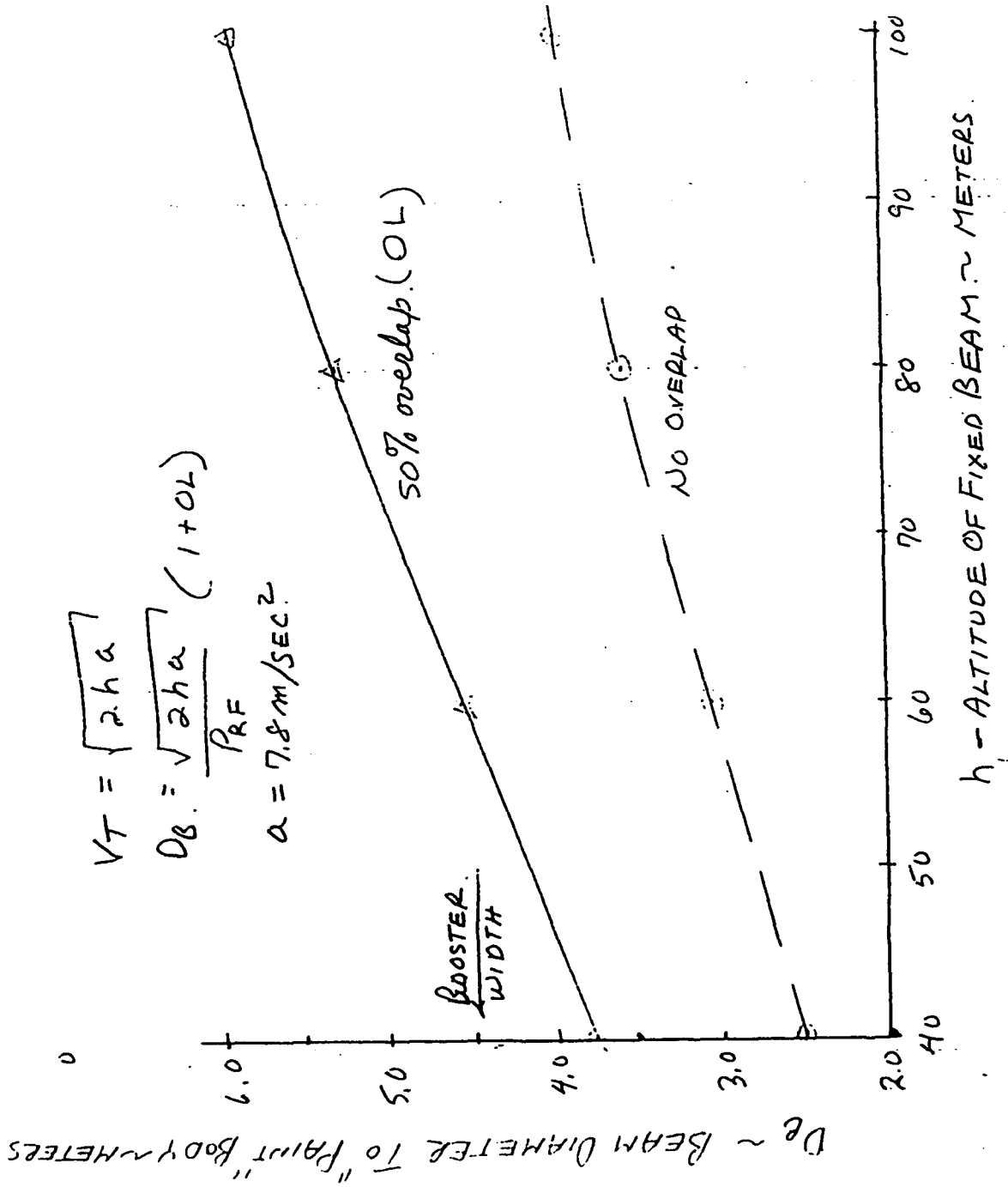
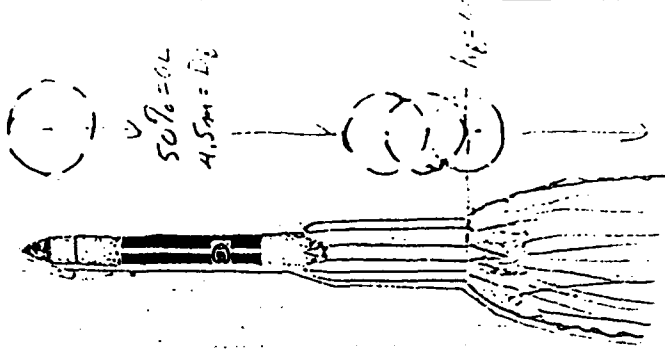


Figure 4. Kinematic implications.



DELTA TARGET

$$a = \left(\frac{I}{W} - 1\right) g = 7.78 \text{ m/sec}^2$$

TARGET LENGTH = 40m

THRUST = 860 Klbs

WEIGHT = 484 Klbs

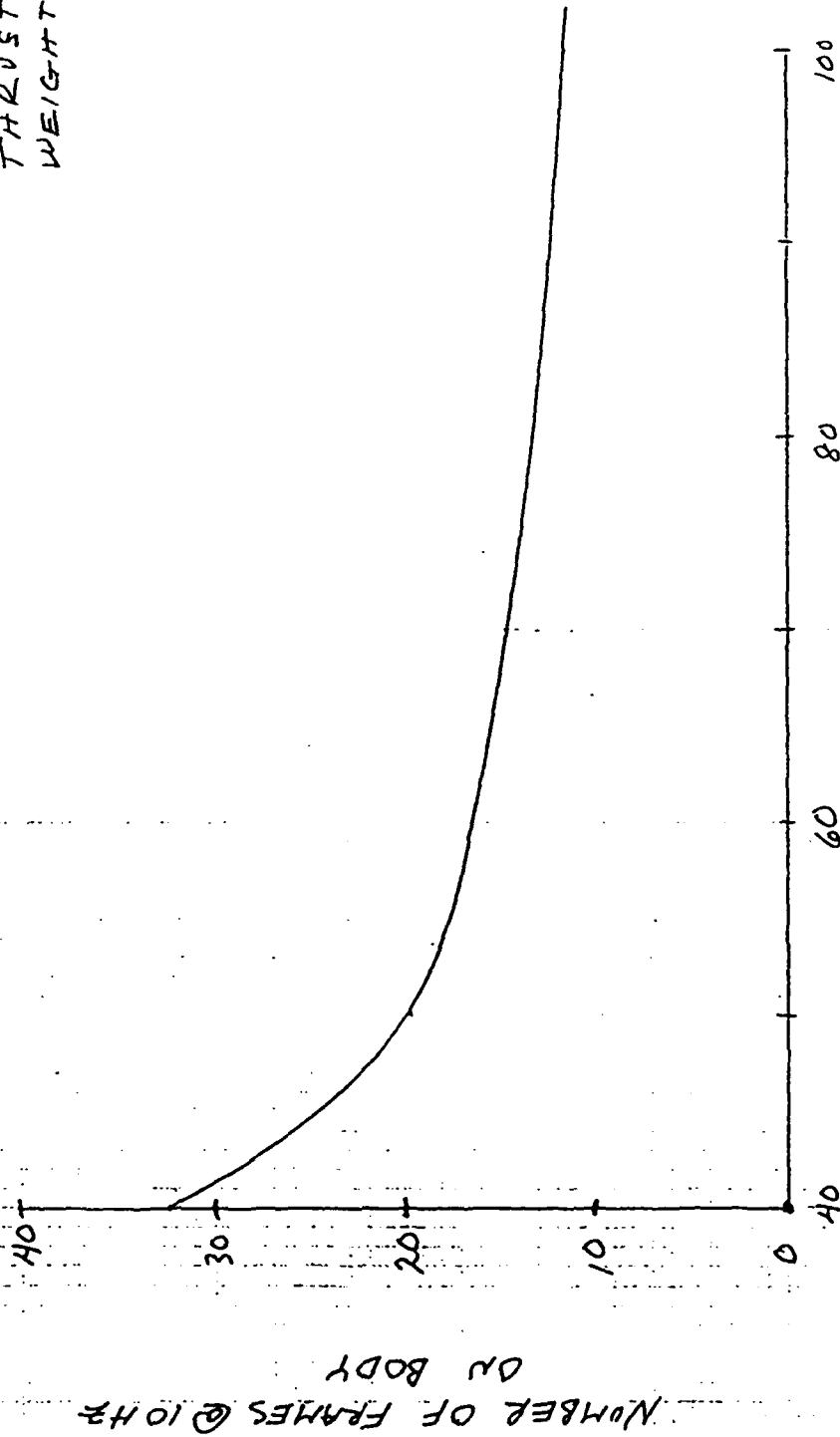


Figure 5. Data quantity (kinematic implications).

- STAGE 1: no tracking; no Doppler signatures; limited to lift-off episode
- Experiment 1
 - Calibrated hard body and plume returns at 0.53 and 1.06
 - Demonstration of resolved A-A texture imaging at 0.53
 - Experiment 2
 - Calibrated hard body and plume returns at 0.53 and 1.06
 - Resolved A-A texture images of hard body and plume at 0.53
 - trailing edge signature
 - STAGE 2: tracking; Doppler signatures; signatures vs. altitude
- Experiment 3
 - Some A-A resolved texture images
 - Some Doppler signatures at 0.53
 - Cross-section at 1.06
 - Experiment 4
 - auto-track
 - Detailed mapping of Doppler signatures of plume at 0.53
 - A-A texture imaging at 0.53
 - Cross-section at 1.06

Figure 6. EOS step-by-step approach to data collection (PDR).

Data Collection Plan:

- Calibrated hard body and plume return @ 0.53 and 1.06
- Demonstration of spatially resolved texture imaging @ 0.53

Implementation:

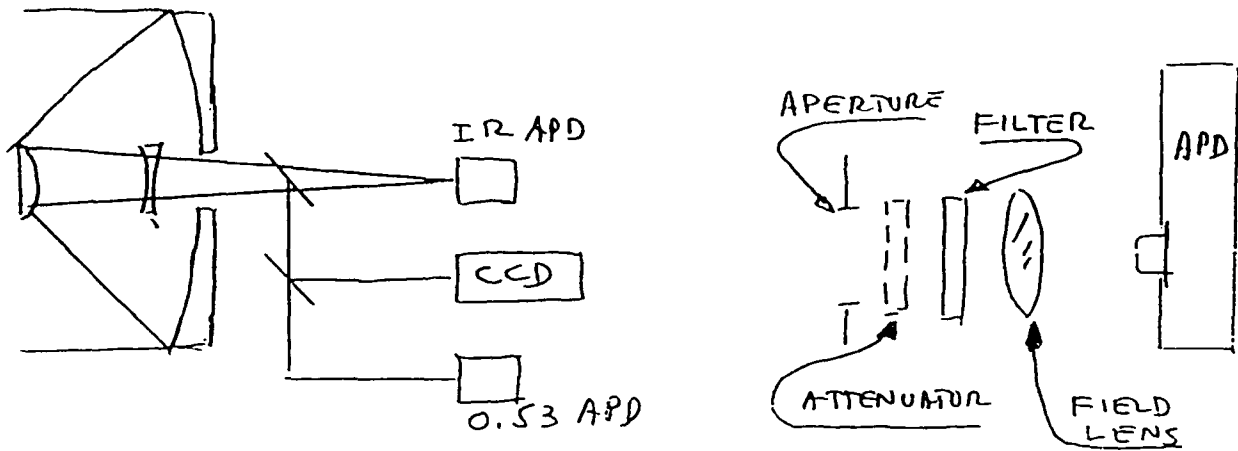
Fixed Illuminator pointing
No beam forming ~2 meter spot
Vehicle moves through fixed beam
0.5 meter collector
Unresolved 0.53 and 1.06 detectors
Gated ICCD camera

Additional Plan:

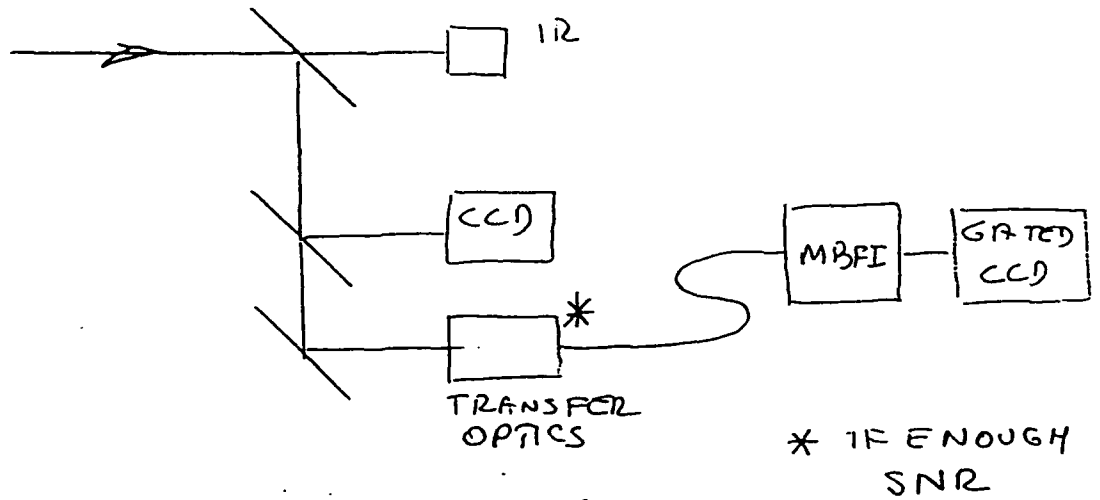
Manual track
Range data

Figure 7. Experiment 1: No tracking, 2-m spot.

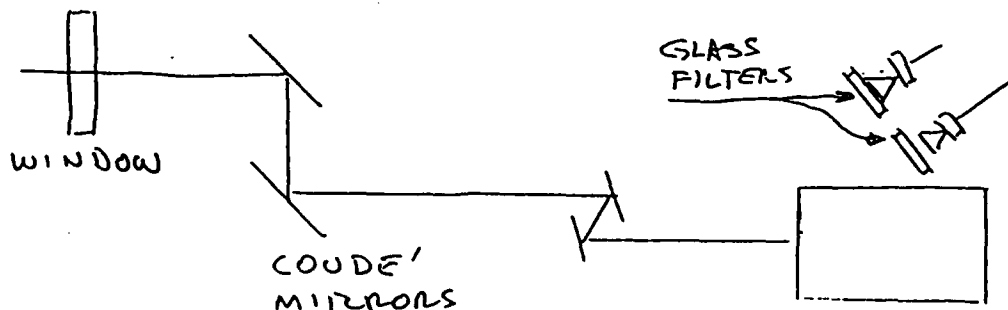
Figure 8. OPTICAL SCHEMATIC



EXPERIMENT 1



EXPERIMENT 2/3



TRANSMITTER

Figure 9.

EXPERIMENT 2: NO TRACKING, 5 m SPOT

- Data Collection Plan:**
- Complex target return, glints, etc.
 - Calibrated target cross-section at 0.53 and 1.06
 - Spatially resolved texture image of target at 0.53
 - Doppler interferometric measurements*

- Implementation:****
- Beam forming optics
 - Beam size @ 0.53 increased 2 m*
 - Beam size @ 1.06 increased 5 m*
 - Match detector FOV to beam
 - Other parameters same as Experiment 1

- Additional Plan:**
- Continue manual track
 - Programmed trajectory with range update

- Comment:**
- If signal levels to photodectors are high, replace 0.53 ADP with optical fiber to MBFI with gated camera

* Additions

** If beam forming optics will delay program, omit expanders, use Experiment 1 beams with MBFI in green.

HARDWARE

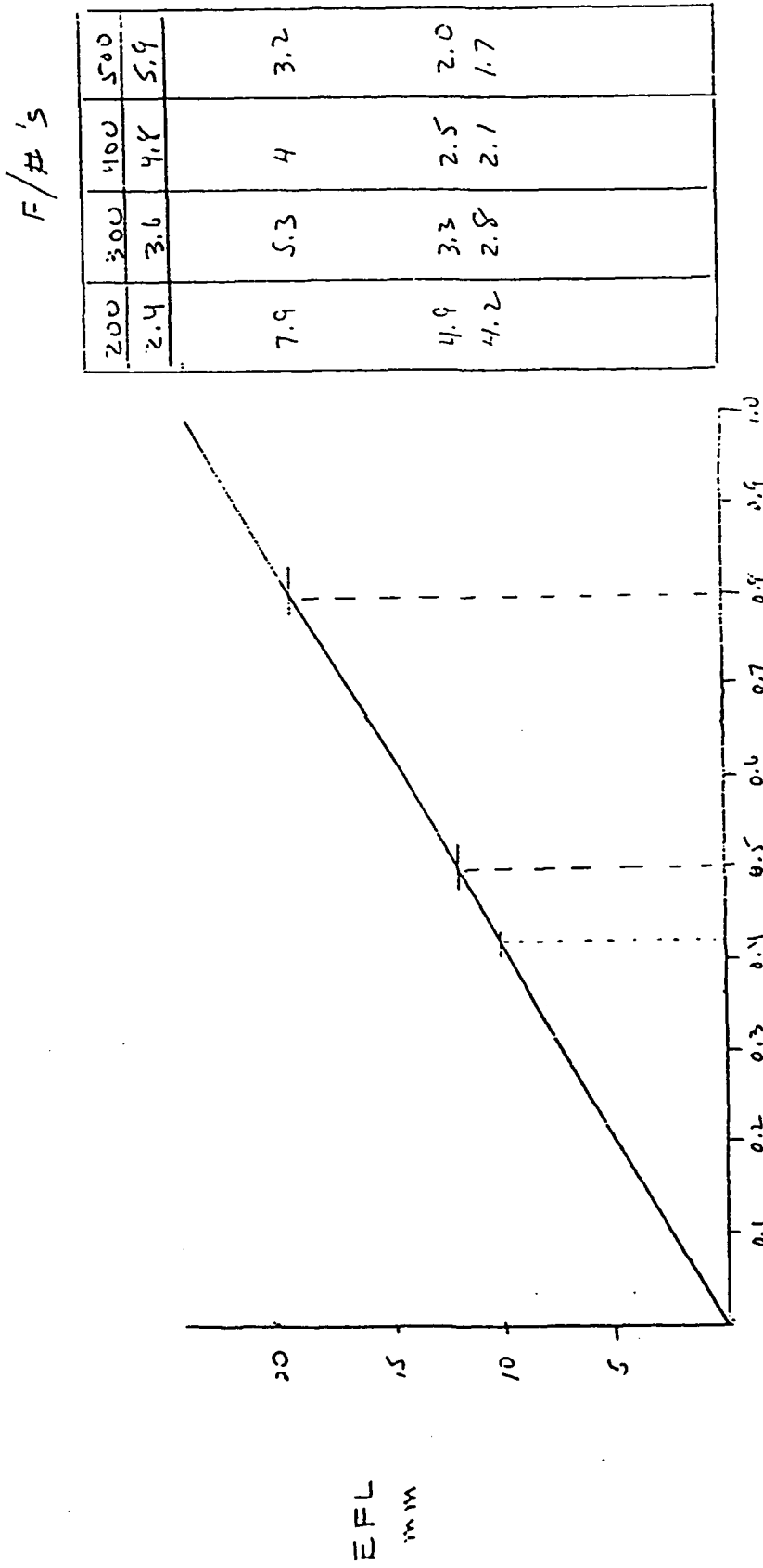
DETECTORS
BEAM SPLITTERS (1")
FILTERS, INTERFERENCE
FILTERS, GLASS
FOCAL PLANE PACKAGE
LIGHT SHIELD, SEPARATE COVER
TELESCOPE COMPONENTS, REVIEWED, ON ORDER
WINDOW
MIRRORS
BARLOW LENS
TELESCOPE MEASUREMENTS
FOCAL PLANE ADJUSTMENTS
BARLOW - FOCUS
INCLUDE X-Y IN DESIGN

Figure 10. Hardware for Experiment 1.

Figure 11.

DETECTOR PACKAGES

- APD's RECEIVED & MODIFIED
- INTERFERENCE FILTERS RECEIVED (0.5")
- FIELD LENSES
 - IR DETECTOR 0.8 mm 19 mm efl
 - GREEN 0.5 mm 11.8 mm
 - USE 10 mm doublet MELLES GRIOT 01LA0001 (6 mm diameter)
- MECHANICAL DESIGN IN PROGRESS
(DETECTOR ASSEMBLIES RCD 2/11/92)



DETECTOR SIZE - MM

Figure 12. Field lens parameters.

BEAM SPLITTERS

Figure 13.

22.5° incidence angle

DESIGN

<u>Spec</u>	λ	R_s	R_p
0.532	10/90	11.67	8.19
		11.67	8.19
0.532	20/80	22.64	17.33
		22.65	17.38
0.532	50/50	54.41	45.82
		54.41	45.91
0.532/1.064	.532	99.9	99.9
	1.064	97	90

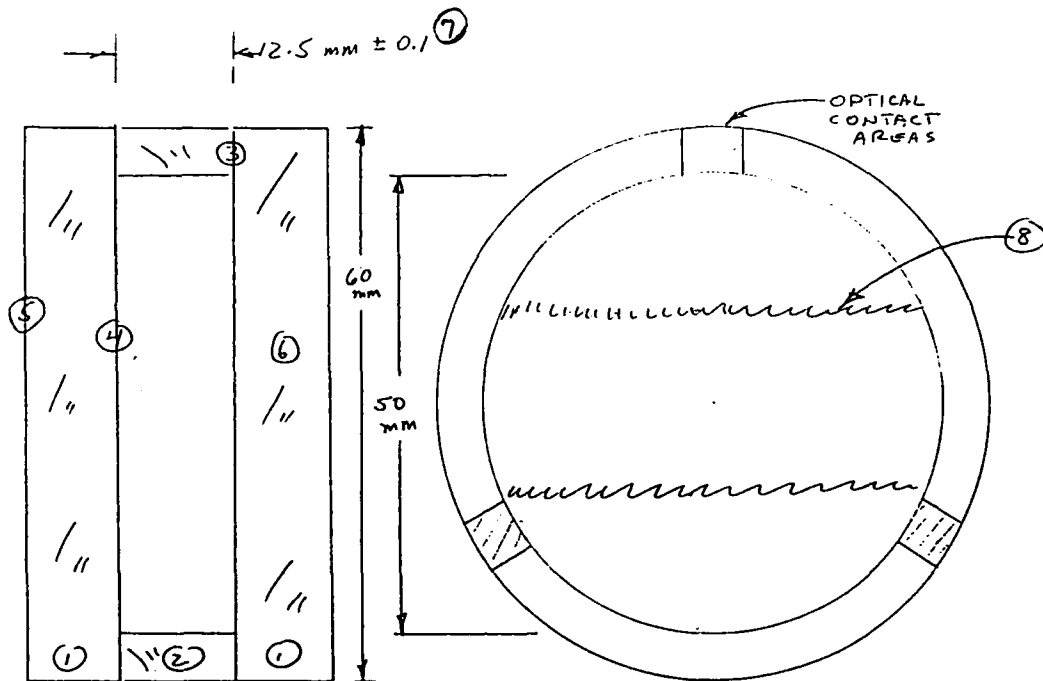
MEASURED

0.532	10/90	9.8
	20/80	21.1
	50/50	52.3

Dichroic

R = 99.7 @ 0.532

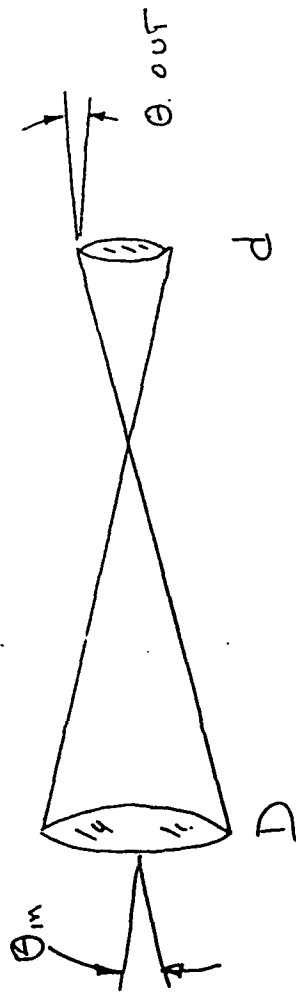
T = 92.5 @ 1.064



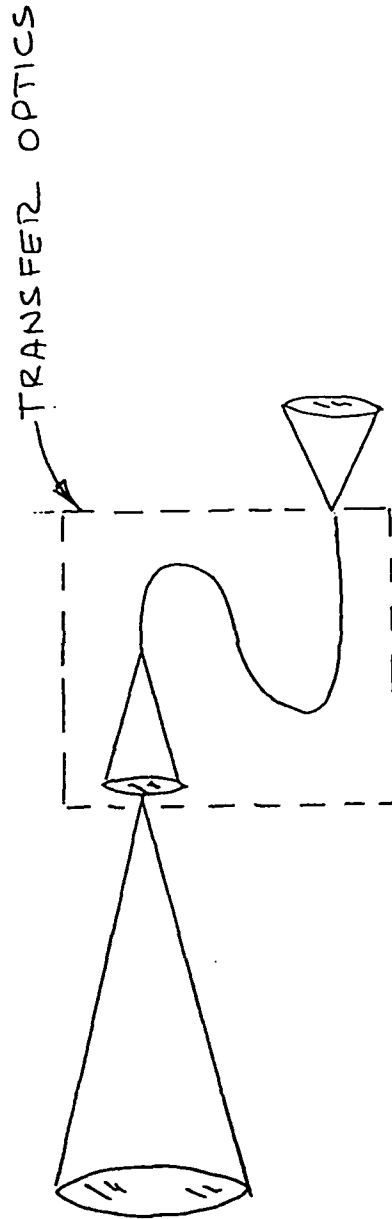
1. Mirror material: Optical fused silica Homosil or equivalent
2. Spacer material: Zerodur, ULE or equivalent
3. Mirrors to be optically contacted to spacer
4. Mirror surfaces: matched to better than $\lambda/120$, after coating, over central 48 mm
 $R = 0.93-0.95 @ 0.53 \text{ \& } 0.63 \text{ \mu m}$
5. Surface flatness: $\lambda/20$ over central 50 mm
 $R < 0.0025 @ 0.53 \text{ \& } 0.63 \text{ \mu m}$
6. Wedge in mirror substrates: 5-30 arc minutes
 Mirrors must be identical and mounted with opposed wedge angles such that the net deviation of a transmitted beam through the etalon is less than 10 arc seconds.
7. Spacer thickness to be measured $\pm 0.0025 \text{ mm}$
8. Spacer to have a wedge of 3.3 arc seconds $\pm 10\%$
 This can be inspected by illuminating the etalon with an expanded, collimated laser beam @ 0.633 \mu m . The fringes seen in transmission shall be spaced by $20 \text{ mm} \pm 2 \text{ mm}$.

Figure 14. Air-spaced wedge etalon.

Figure 15. RECEIVER OPTICS FOR AUTODYNE



$$\theta_{out} = \theta_{in} \times \frac{D}{d}$$



TRANSFER OPTICS MATCH F/# & APERTURE

WHAT LIMITS θ_{out} ?

$R_1 = R_2 = 0.93$
 $T_1 = T_2 = 0.07$
 $\alpha = 16 \mu\text{rad}$
 $\lambda = 0.532 \mu\text{m}$
 $\theta_s = 1.00 \text{ mrad}$

Transmission Fringe Sensitivity to θ_0

Nominal Order = 37568; FSR = 15 GHz

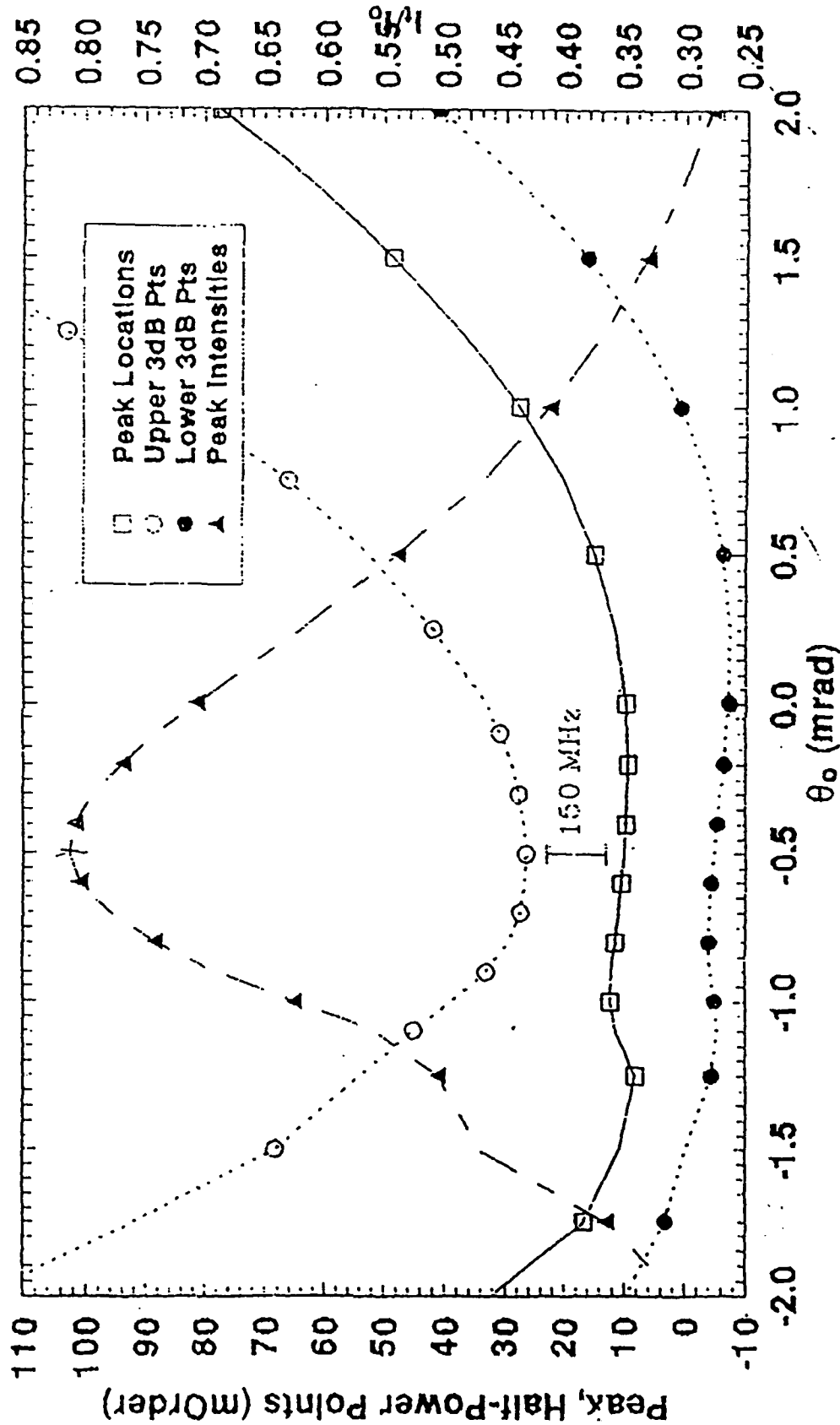


Figure 16. Transmission fringe sensitivity to incidence angle.

$R_1 = R_2 = 0.94$
 $T_1 = T_2 = 0.06$
 $\alpha = 16 \mu\text{rad}$
 $\lambda = 0.532 \mu\text{m}$

Transmission Fringe Sensitivity to θ_s Nominal Order = 47000; FSR = 12 GHz

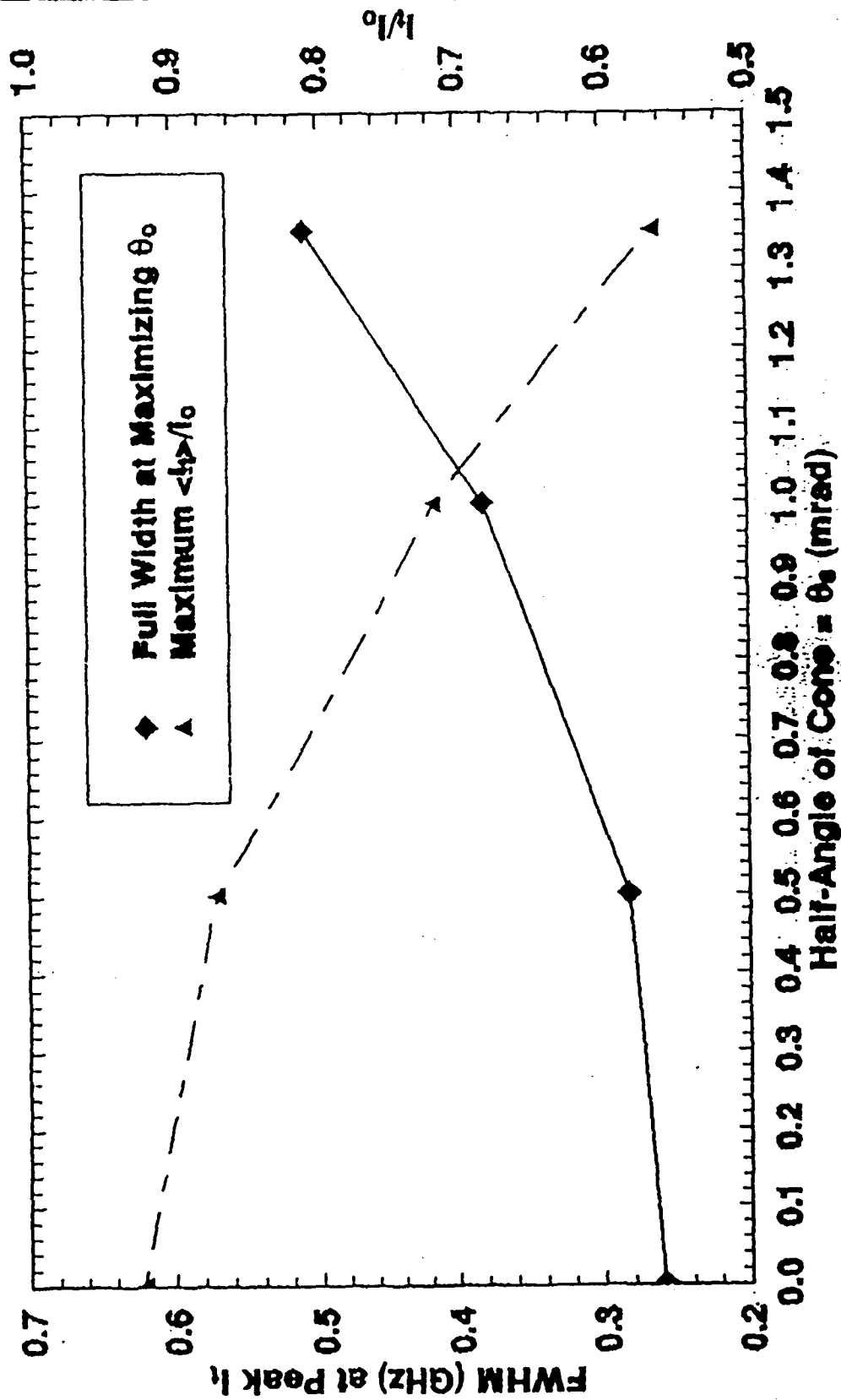
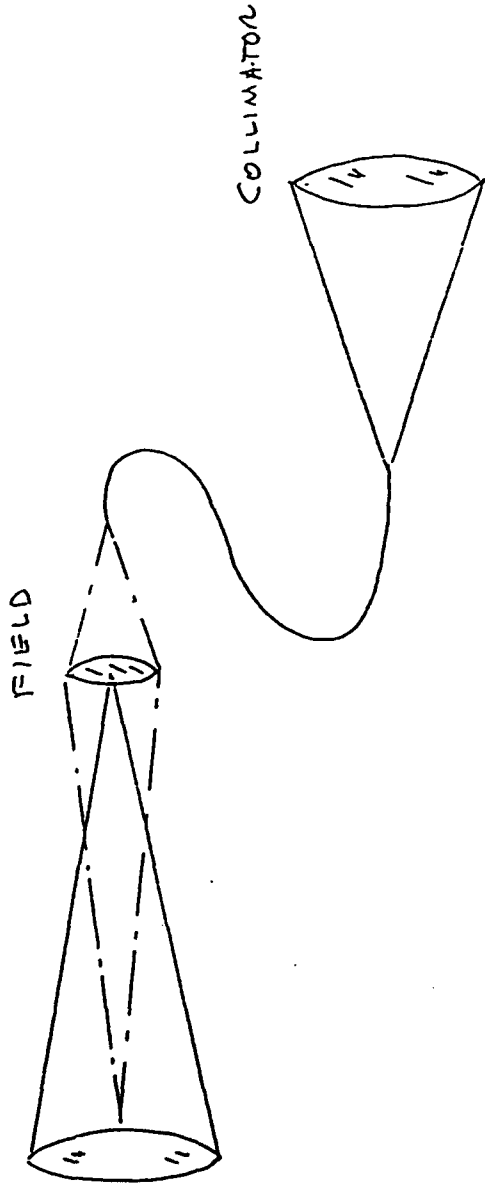


Figure 17. Transmission fringe sensitivity to field of view.



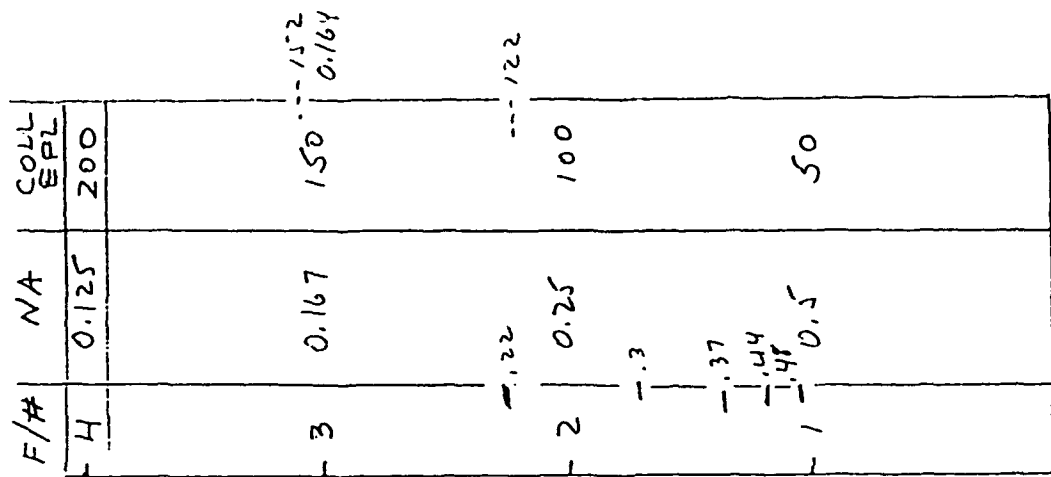
$$\frac{\text{COLLIMATOR EFL}}{\text{FIELD EFL}} = \frac{\text{COLL D}}{\text{FIELD D}}$$

$$\text{DIAMETER FIELD} = 0.2 \text{ MRAD} \times 11.875 \text{ m} = 2.375 \text{ mm}$$

$$\text{DIAMETER COLLIMATOR} = 50 \text{ mm}$$

$$\text{RATIO} \quad 50 / 2.375 = 21.05$$

Figure 18. Transfer optics -- field-of-view considerations.



$$F/\# = \frac{EFL}{200 \mu\text{RAD FIELD}}$$

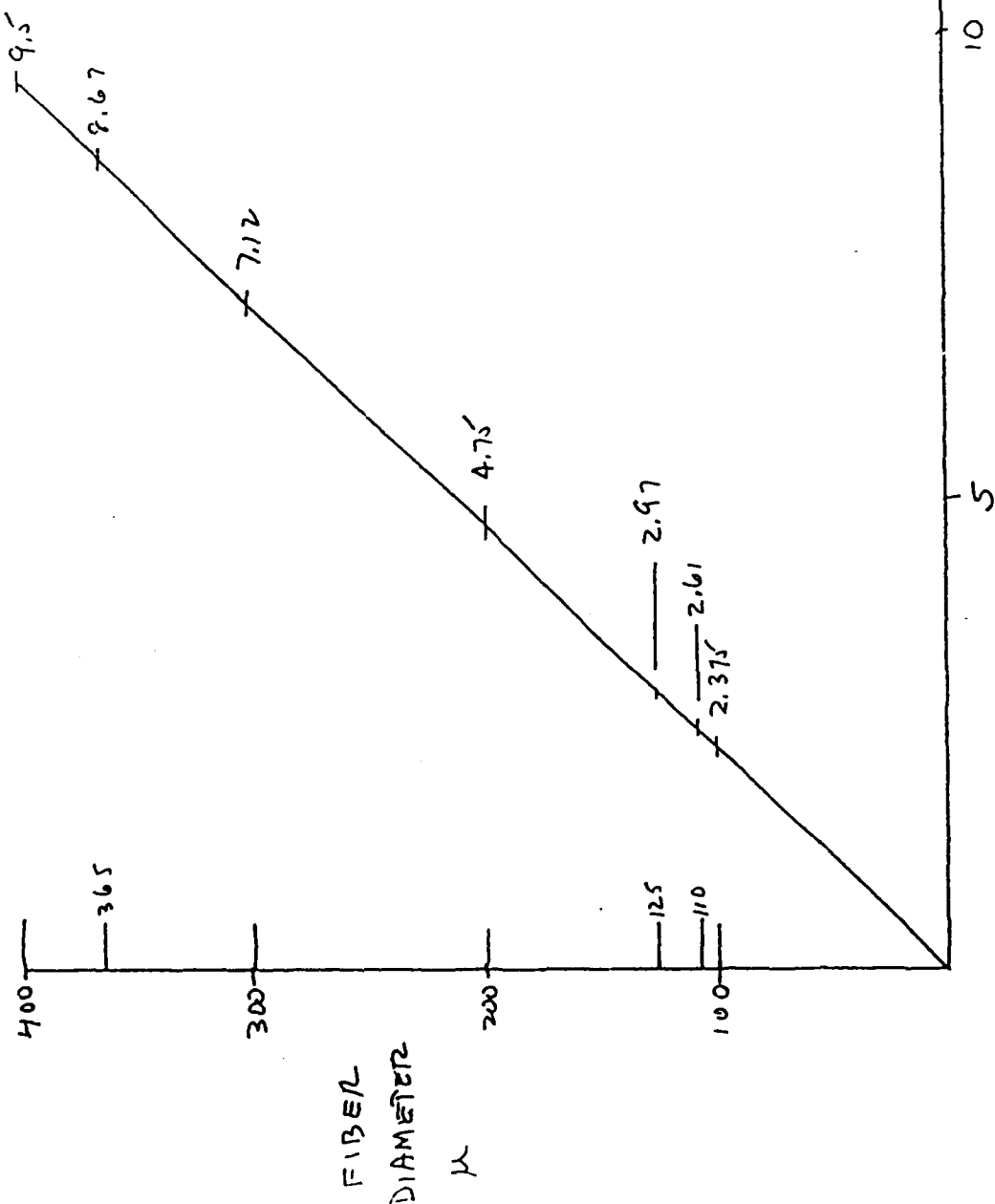
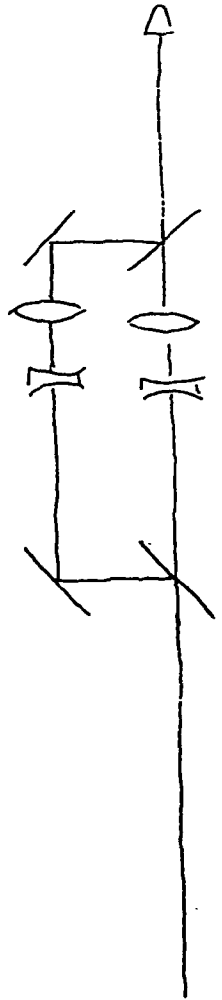


Figure 19. Transfer optics -- parameters.



• INDEPENDENT CONTROL
1.064 & 0.53

• CONNECTION - COLLINEARITY

Figure 20. Beam Expander concept.

Figure 21.

BEAM EXPANDER FOR AUTODYNE EXPERIMENTS

- TARGET REFLECTANCE MEASUREMENTS
PAINT TARGET WITH 5 METER BEAMS (OVERLAP)
- DOPPLER MEASUREMENTS
LIMIT TO 2 METER BEAMS
- UNMODIFIED LASER (OLD DATA)
GREEN 1.5 X 2.5 METER
IR 3.3 X 4.0 METER
- BEAM SPLIT WITH INDIVIDUAL EXPANDERS
DELIVERY
- FALLBACK
GO UNMODIFIED WITH SLIGHT SIGNAL LOSS

Figure 22.

ELECTRONICS BLOCK DIAGRAM

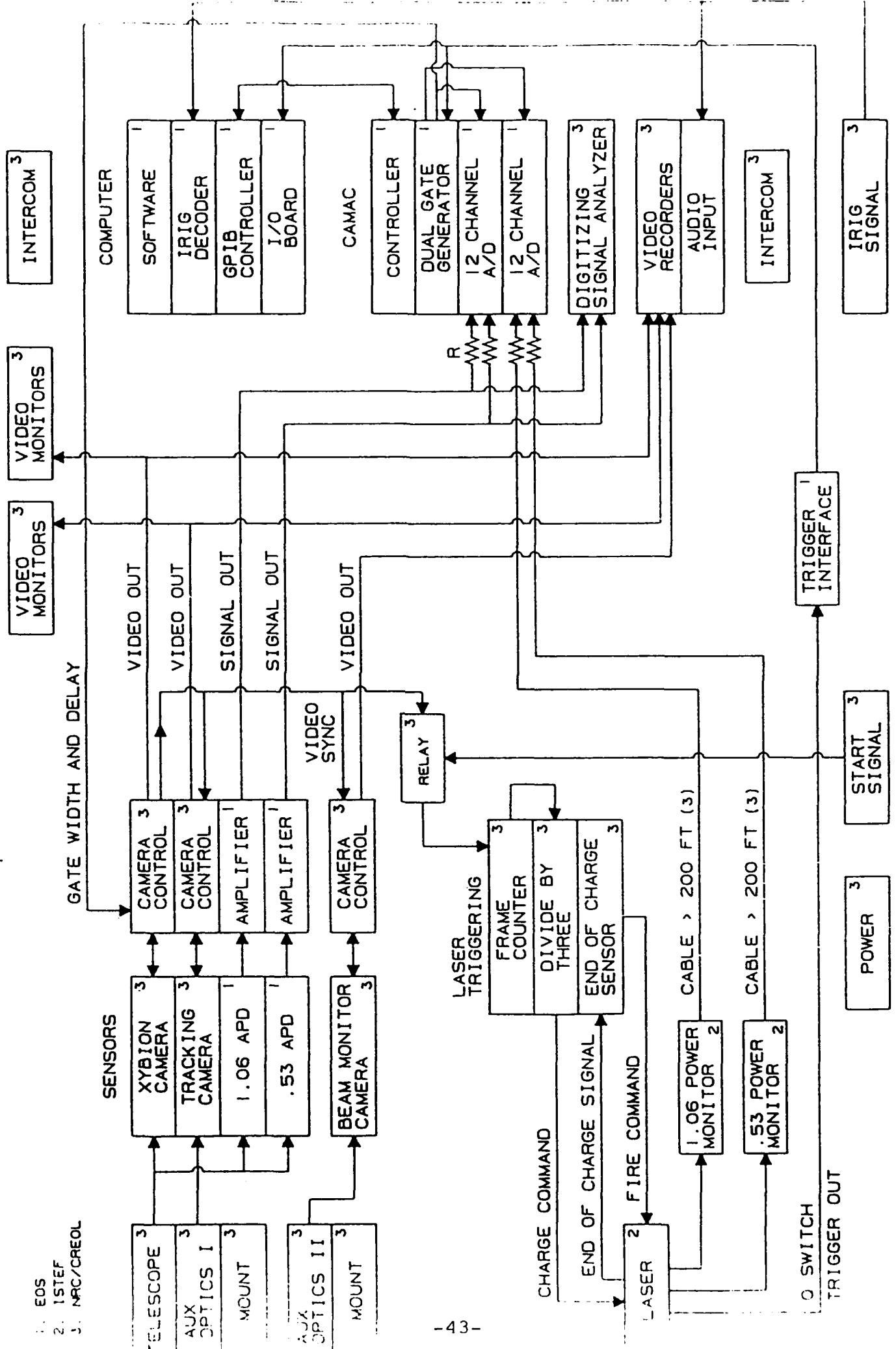
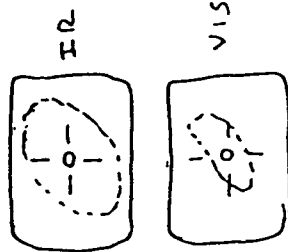
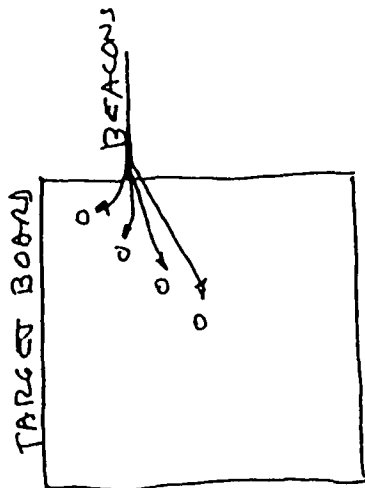


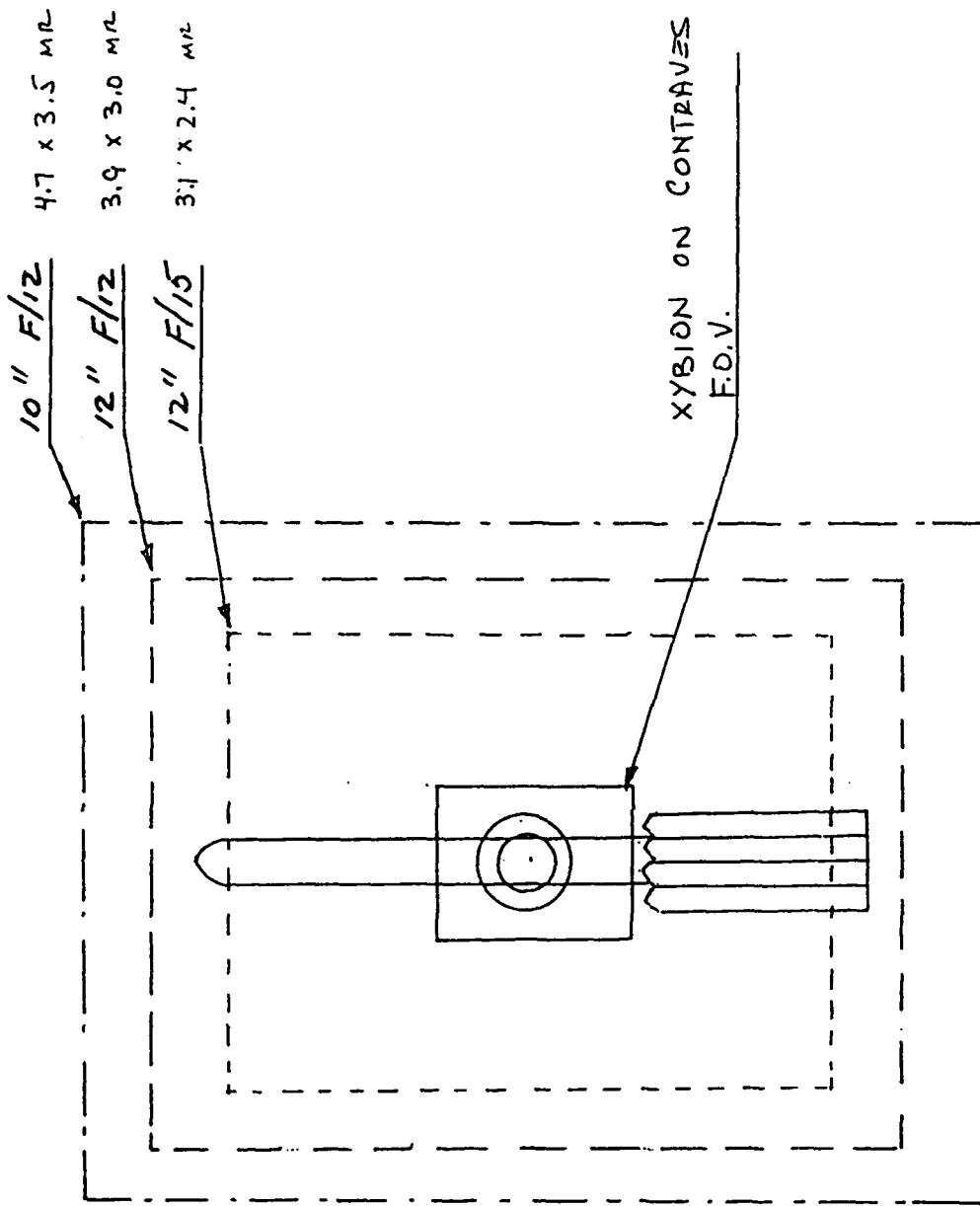
Figure 23. Calibration.

- o COLLINEARITY OF 1.06 μ 0.53 @ 10 KM
- o FAR FIELD DISTRIBUTION
- o USE ANCILLARY VISIBLE & IR SENSORS TO OBSERVE TGT BOARD
- o ALIGN EACH CAMERA TO CENTER BEACON
- o MEASURE SPOT LOCATION WITH RESPECT TO RETICLE
- o ADDITIONAL BEACONS USED FOR R-O MEASURE
- o ATMOSPHERIC TRANSMISSION
- o BORESIGHT PHOTO BOCKETS WITH LASER TRANSMITTER

TARGET $\rho \sim 0.3/sr$, - WITHOUT FILTERS,
 AT NIGHT, SIGNAL WITH 12" OPTICS
 3X 0.5 METER, IN GREEN



ALIGNMENT
 SENSOR
 IMAGE



ITT - 18 mm DIAG
XYBION 16 mm DIAG

Figure 24.
COMPARATIVE F.O.V. CHART

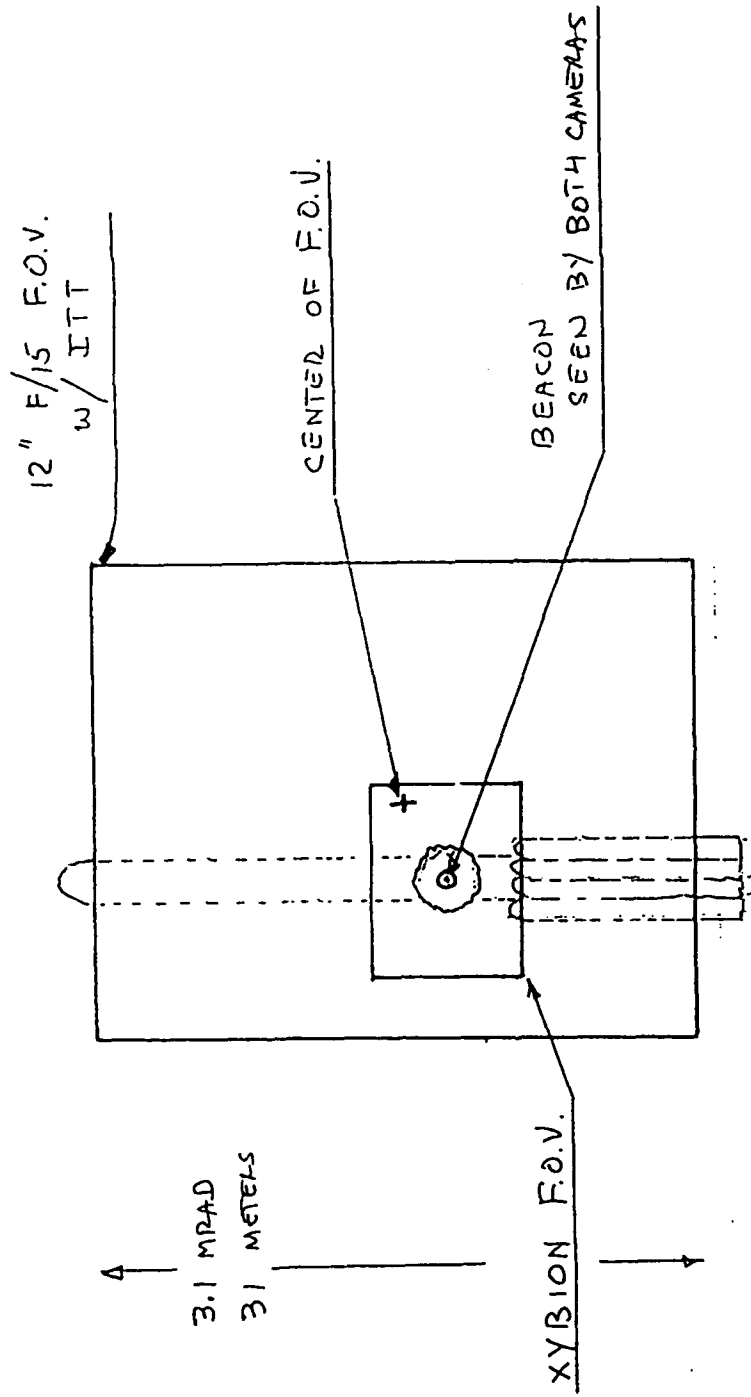
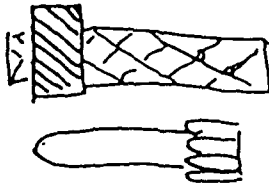


Figure 25.
TARGET BOARD CALIBRATION

Figure 26. Calibration board on gantry.

- BORESIGHT
- KNOWN REFLECTIVITY REFERENCE
- ATMOSPHERIC TRANSMISSION



- PAINTED TARGET BOARD ON GANTRY
- MEASUREMENT @ 0.53 & 1.06
- EXPERIMENT 1 - 2.5 METERS ~ 8 ft
- EXPERIMENT 2 - 4-5 METERS ~ 16 ft MULTIPANEL
- TARGET EXISTS AT 1 KM BUT DIRECTION & RANGE NOT SUITABLE FOR BORESIGHTING & TRANSMISSION MEASUREMENT

TO BE RESOLVED:

- CAN TARGET BE RECORDED & ILLUMINATED?
- RANGE SAFETY
- DOES 100 METER ELEVATION CHANGE MATTER?

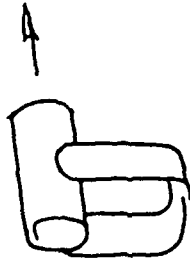


Figure 27.
**Signal Photon Counts
Plume and Hard Body**

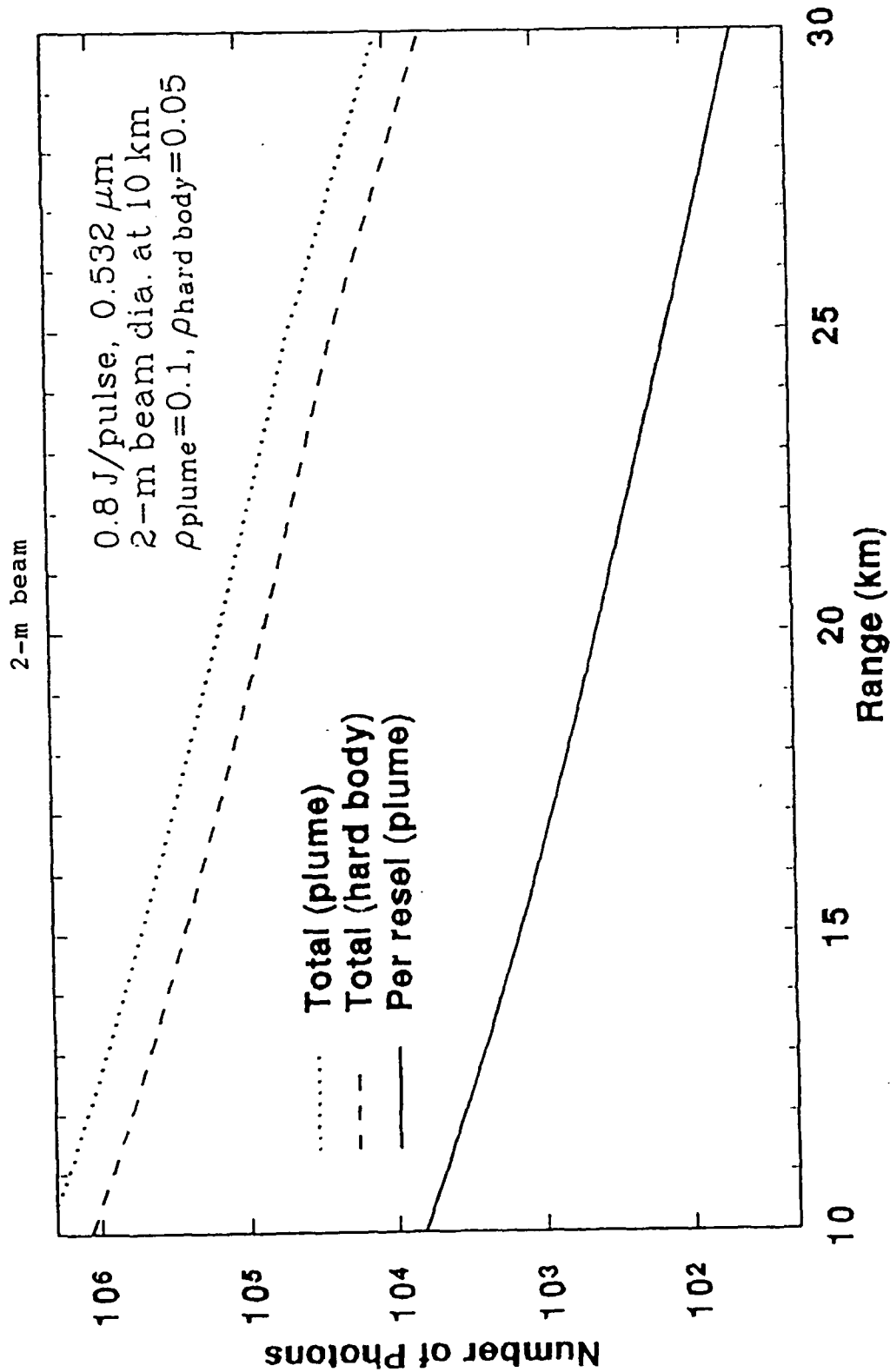


Figure 28. Signal Photon Counts Plume and Hard Body 5-m Beam

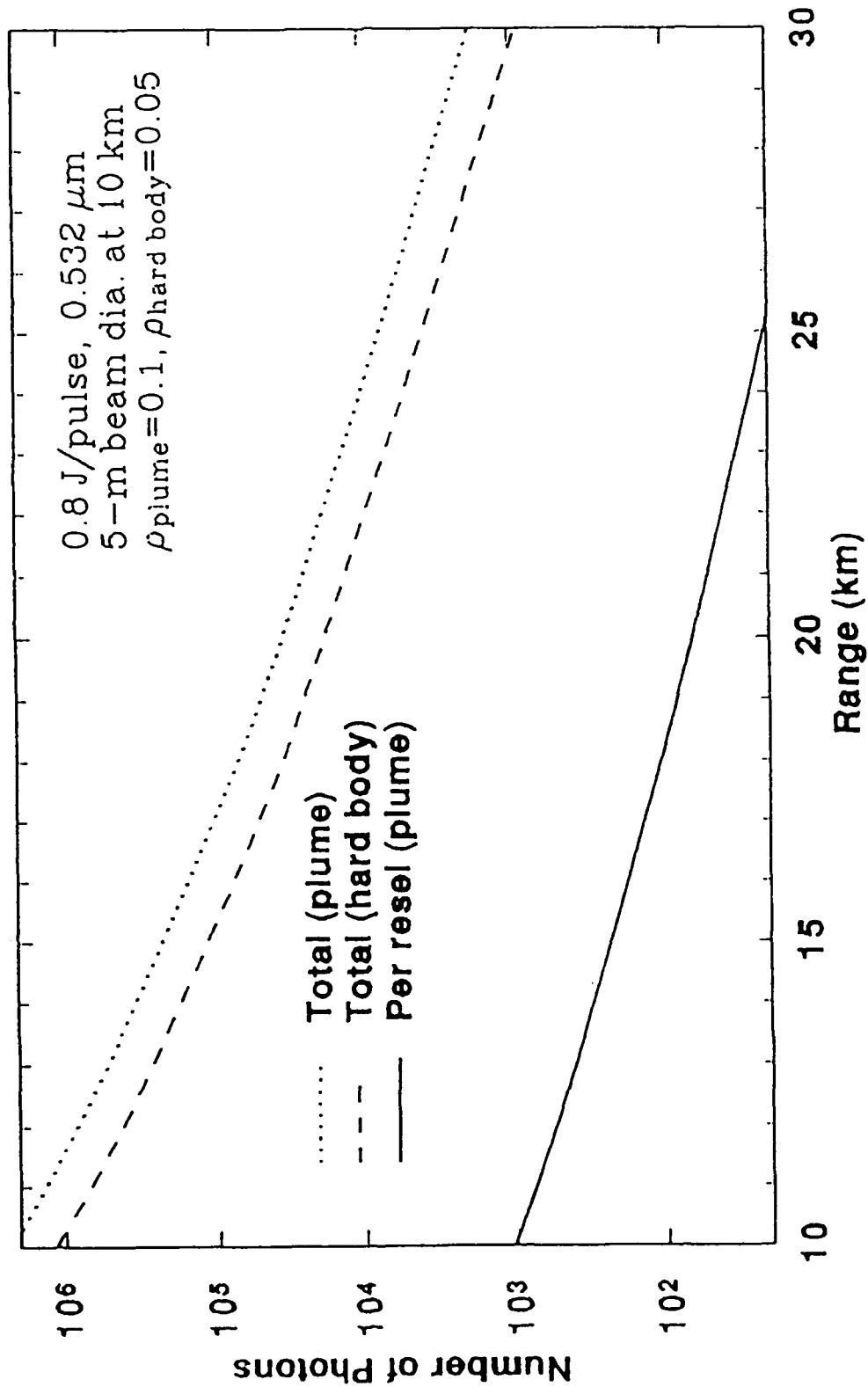


Figure 29.
Background Photon Counts
Plume Fills Receiver FOV

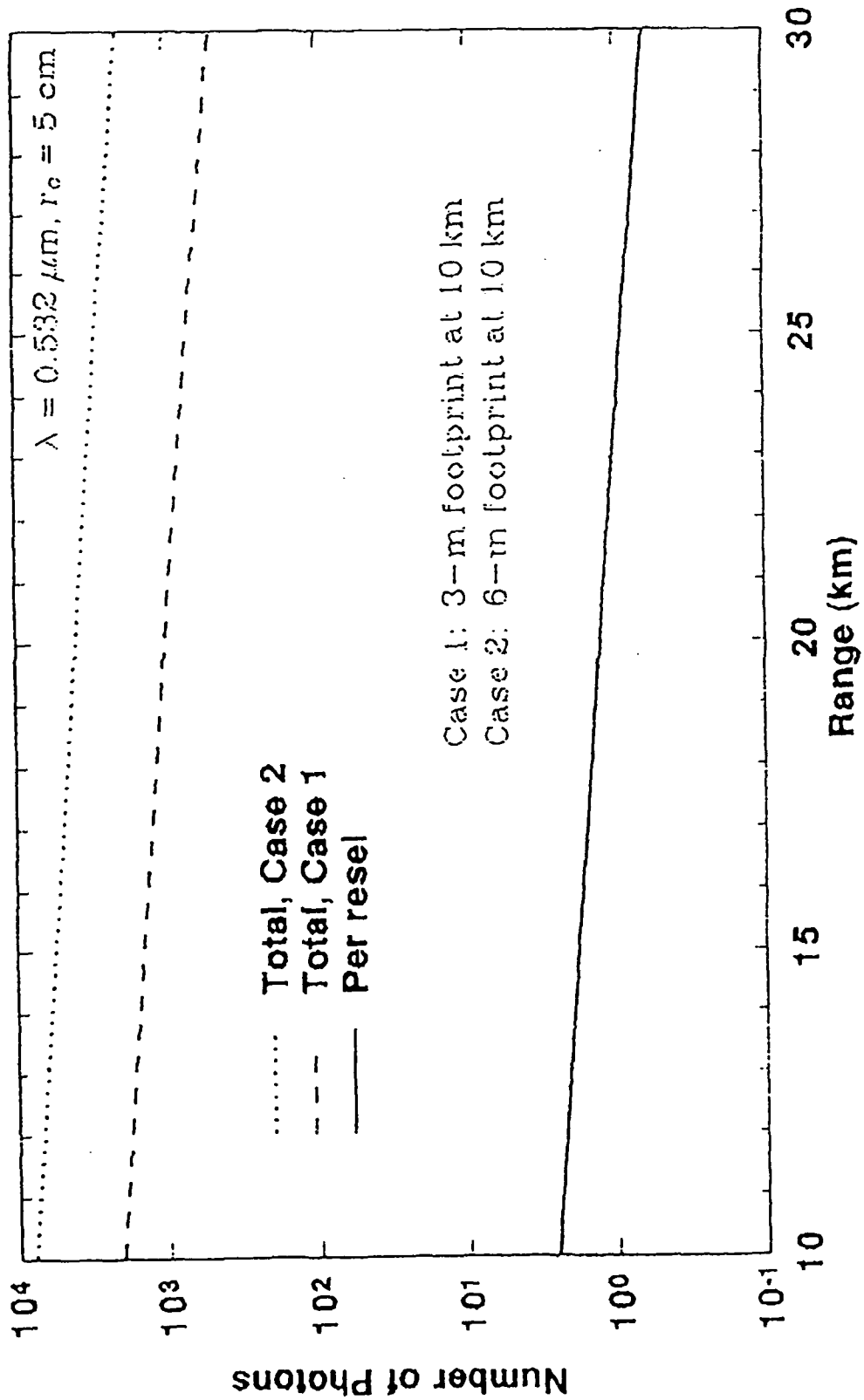


Figure 30.
"Lidar Signal to Noise Ratio" = $\frac{M_s^2}{M_s + M_b}$
Plume Against Plume Background

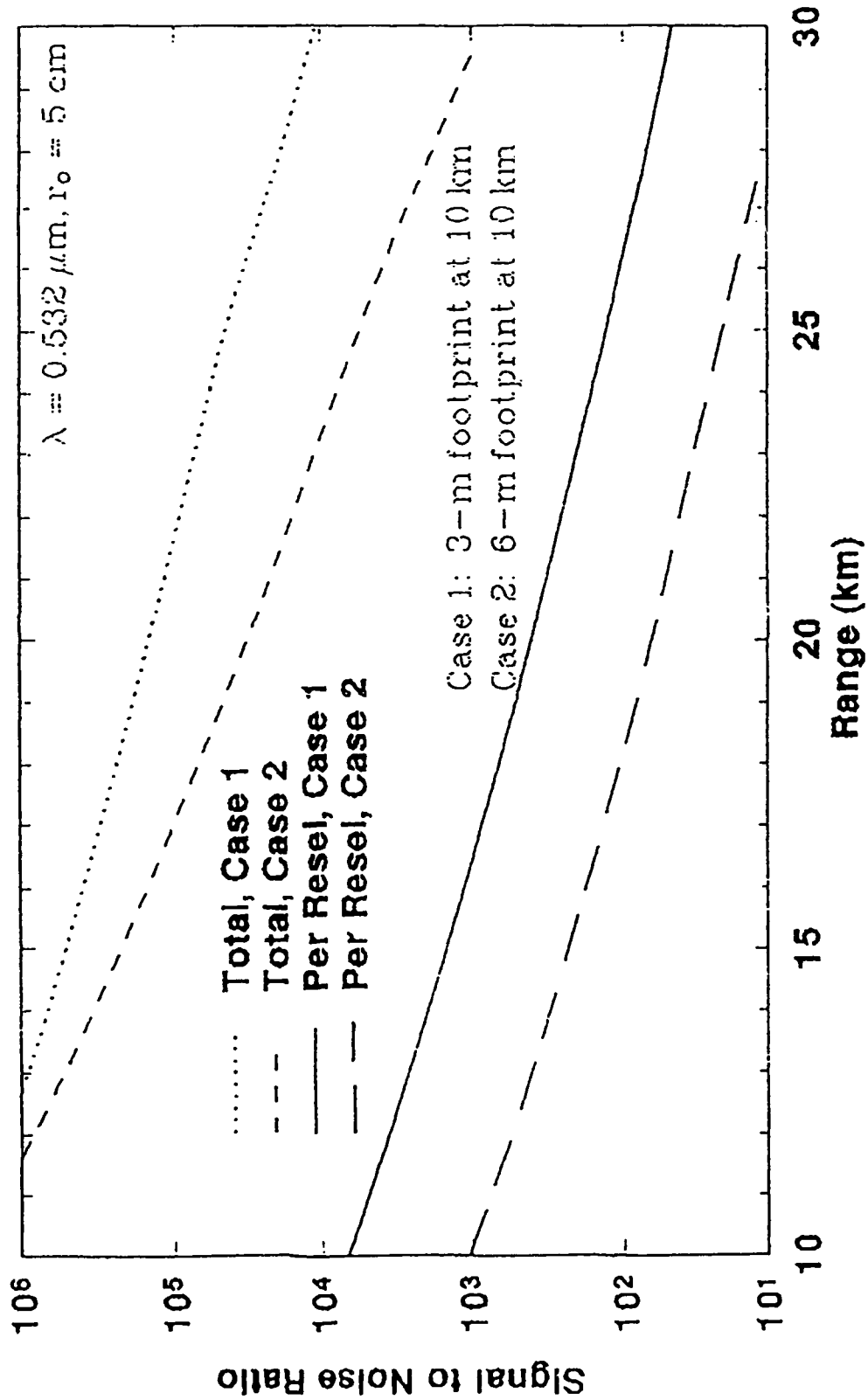
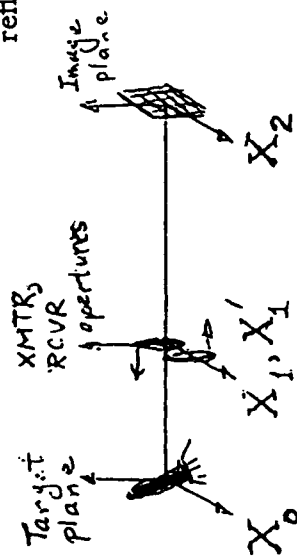


Figure 31.

EXPRESSION FOR SPECKLE CONTRAST

$$\begin{aligned}
 \underbrace{U_k(\mathbf{x}_2)}_{\text{for } k\text{th scatterer at image plane}} &= A \iiint \underbrace{d^2\mathbf{x}_1}_{\text{XMTR aperture}} \underbrace{d^2\mathbf{x}'_1}_{\text{RCVR aperture}} \underbrace{d^2\mathbf{x}_0}_{\text{target plane}} \underbrace{B(\mathbf{x}_0 - \mathbf{x}_1)}_{\text{raw beam amplitude}} \underbrace{G_A(\mathbf{x}_0 - \mathbf{x}_1)}_{\text{turbulence XMTR to target}} \\
 &\cdot \underbrace{\rho(\mathbf{x}_0 - \mathbf{v}_k t)}_{\text{target reflectance}} \underbrace{h(\mathbf{x}_0 - \mathbf{x}_2)}_{\text{RCVR telescope}} \underbrace{G_A(\mathbf{x}_0 - \mathbf{x}'_1)}_{\text{turbulence target to RCVR}}
 \end{aligned}$$



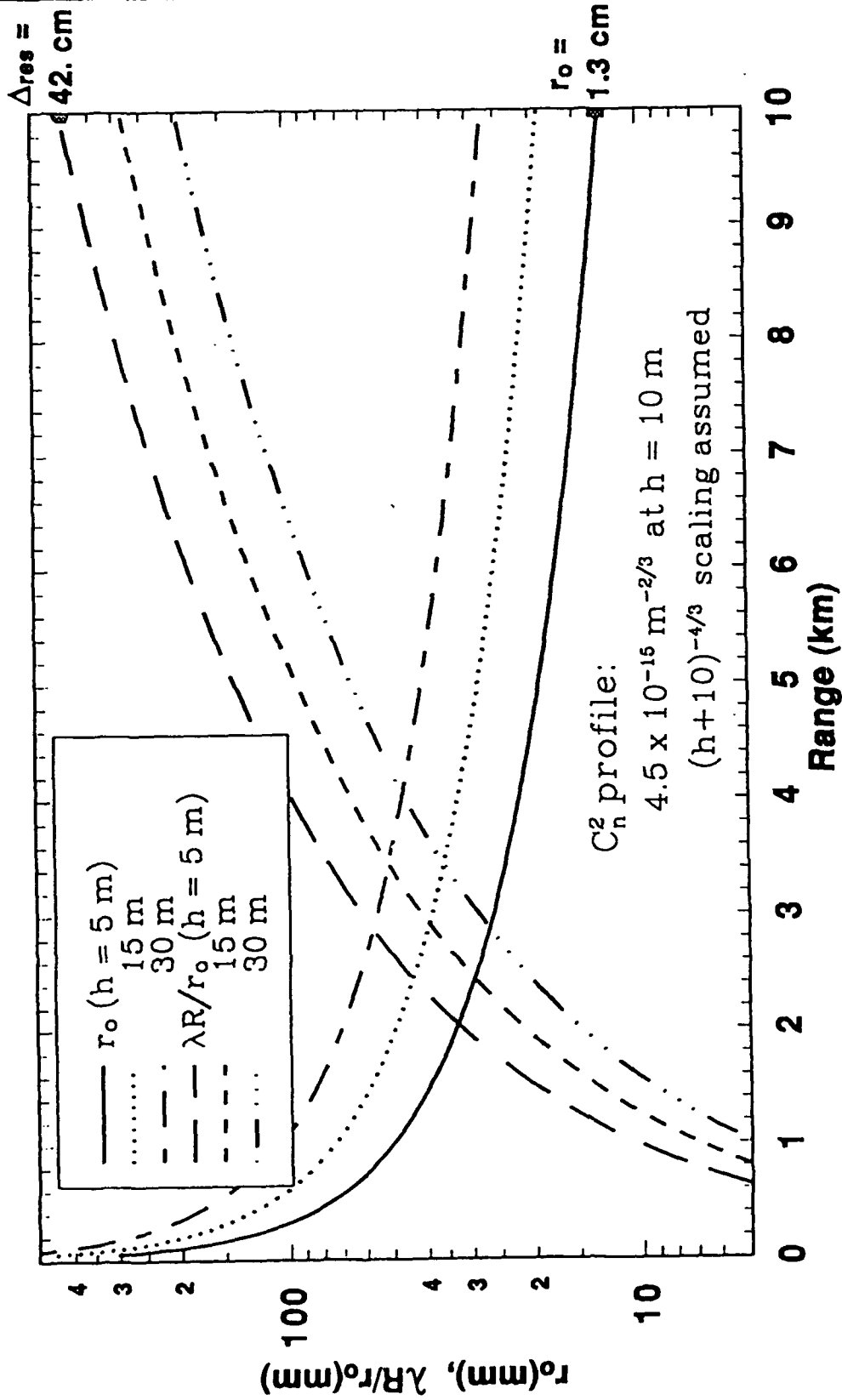
$$I(\mathbf{x}_2) = \left| \sum_k U_k(\mathbf{x}_2) \right|^2$$

$$\langle \rho(\mathbf{x}_0 - \mathbf{v}_k t) \rho(\mathbf{x}'_0 - \mathbf{v}_{k'}(t + \tau)) \rangle > \approx \rho_k^2 \delta(\Delta \mathbf{x}_0 + \Delta \mathbf{v}_k \tau)$$

$$\text{Contrast} = \sqrt{\text{Var}(I(\mathbf{x}_2))} / \langle I(\mathbf{x}_2) \rangle$$

- Triple-product covariance analysis (1974)

Figure 32.
TURBULENCE EFFECTS
 Spherical Waves, $\lambda = 0.532 \mu\text{m}$, Horizontal Paths



TURBULENCE EFFECTS

Spherical Waves, $\lambda = 0.532 \mu\text{m}$, Horizontal Paths

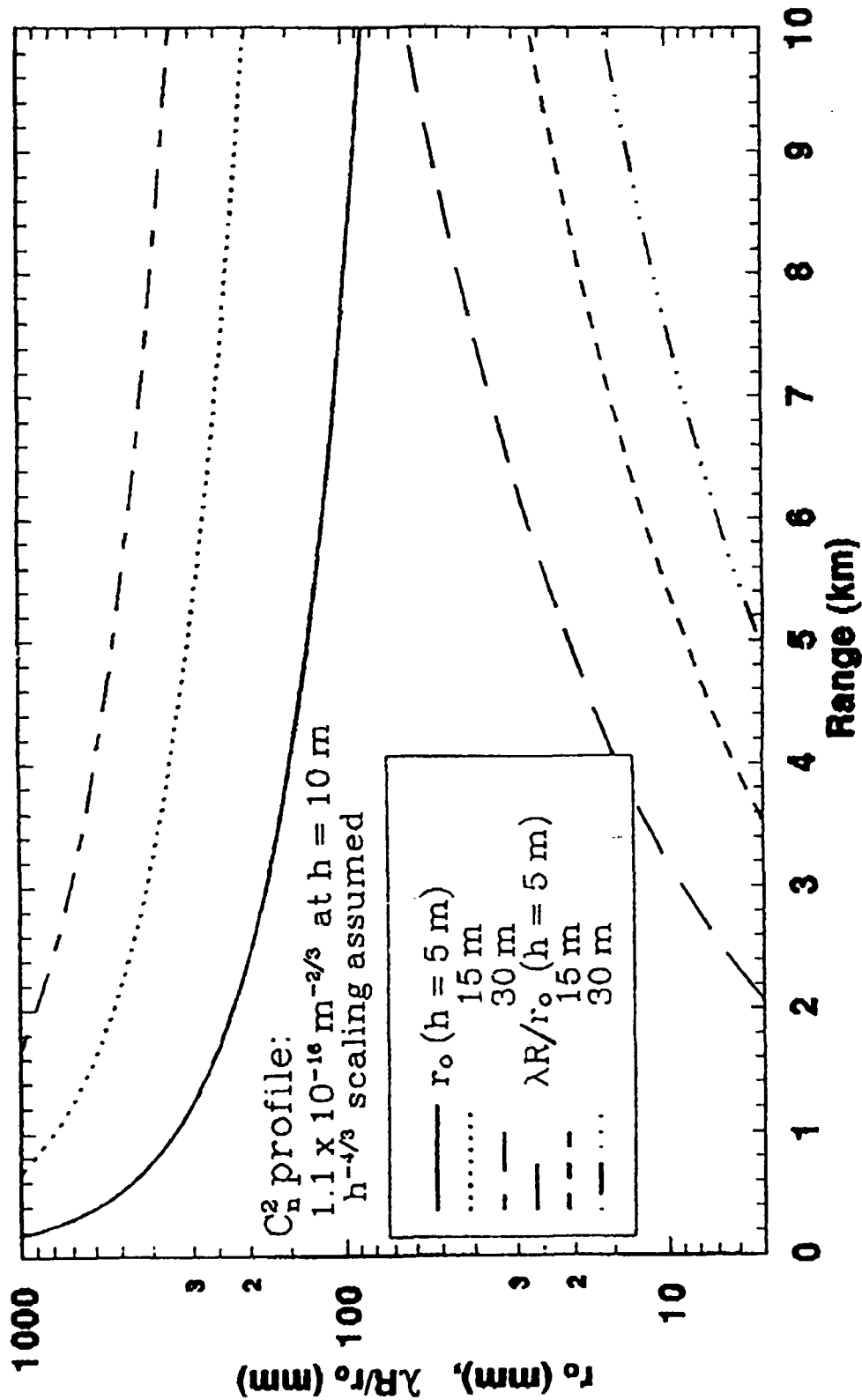


Figure 33. Predictions for very low turbulence.

Figure 34.
TURBULENCE EFFECTS
Spherical Waves, $\lambda = 1.064 \mu\text{m}$, Horizontal Paths

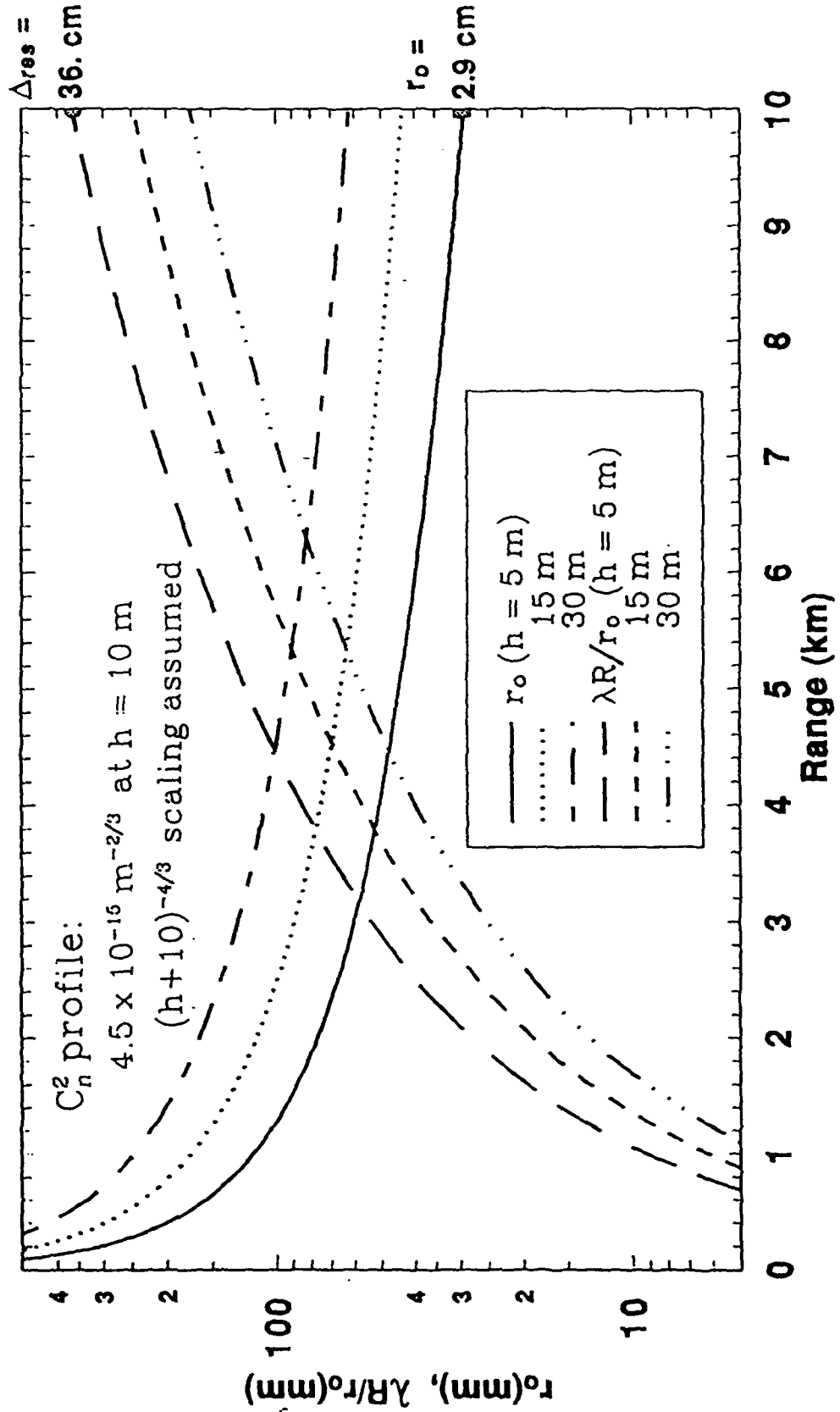


Figure 35.

CONTRAST MODULATION DUE TO BEAM STEERING

Approximate One-Dimensional Analytical Formulation

Nominal Profile: $I(x) = \exp(-x^2/2\sigma^2)$

Displaced Profiles: $I(x \pm \delta) = \exp(-(x \pm \delta)^2/2\sigma^2)$

Nominal Average Over Region $\{x - \Delta/2 \leq x \leq x + \Delta/2\}$:

$$\text{const} \times [\text{erf}((x + \Delta/2)/\sigma) - \text{erf}((x - \Delta/2)/\sigma)]$$

Average (Over Same Region) of Displaced Profile:

$$\text{const} \times [\text{erf}((x \mp \delta + \Delta/2)/\sigma) - \text{erf}((x \mp \delta - \Delta/2)/\sigma)]$$

Contrast Modulation (for special case, $\Delta = \delta$):

$$\frac{[\text{erf}((x + \Delta)/\sigma) + \text{erf}((x - \Delta)/\sigma) - 2 \times \text{erf}(x/\sigma)]}{2 \times [\text{erf}((x + \Delta/2)/\sigma) - \text{erf}((x - \Delta/2)/\sigma)]}$$

Figure 36.
CONTRAST MODULATION DUE TO BEAM STEERING
Gaussian $\sigma = 1.5$ m; $\Delta_{res} = 0.42$ m

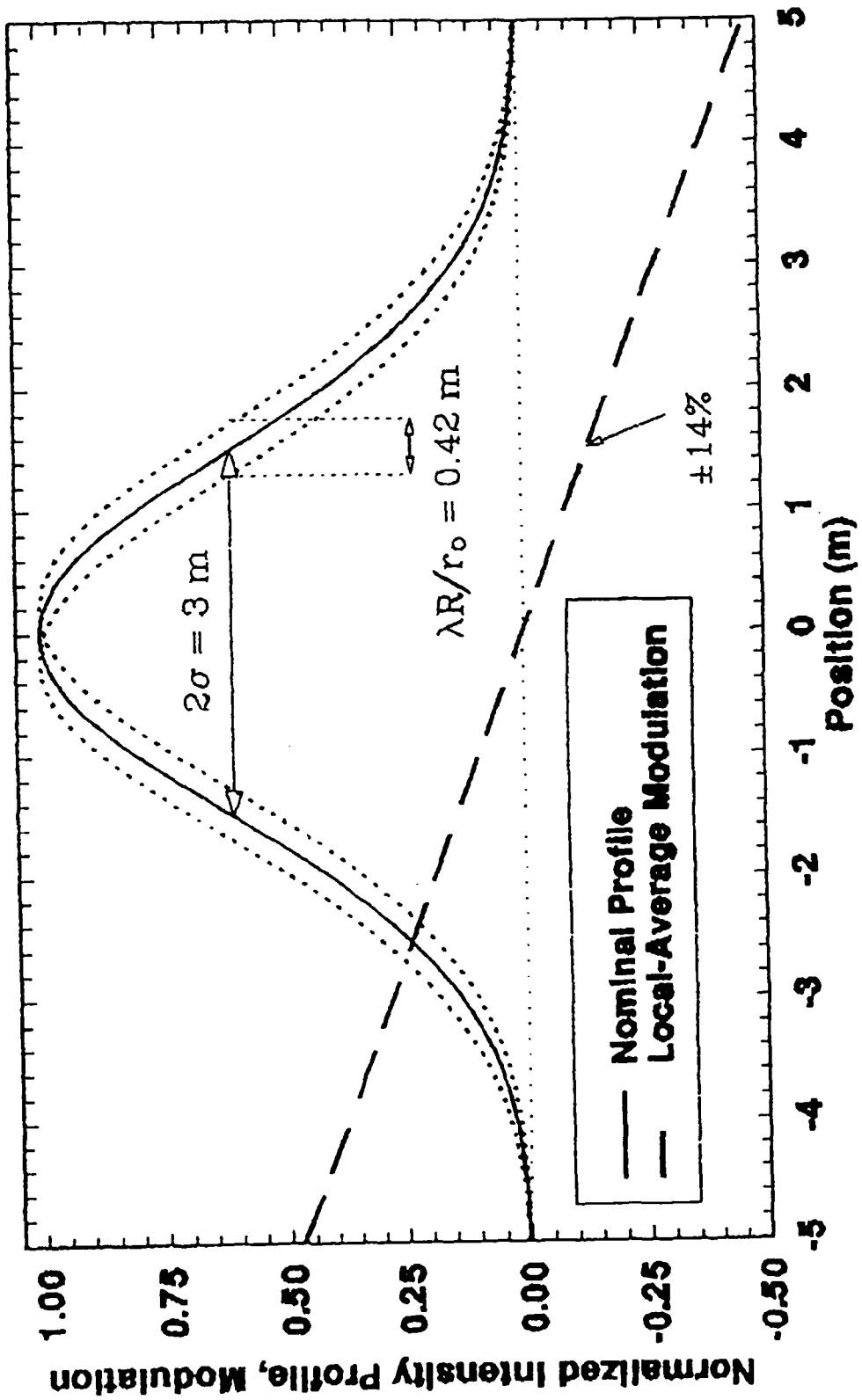


Figure 37.
CONTRAST MODULATION DUE TO BEAM STEERING
Gaussian $\sigma = 2.5$ m; $\Delta r_{oc} = 0.42$ m

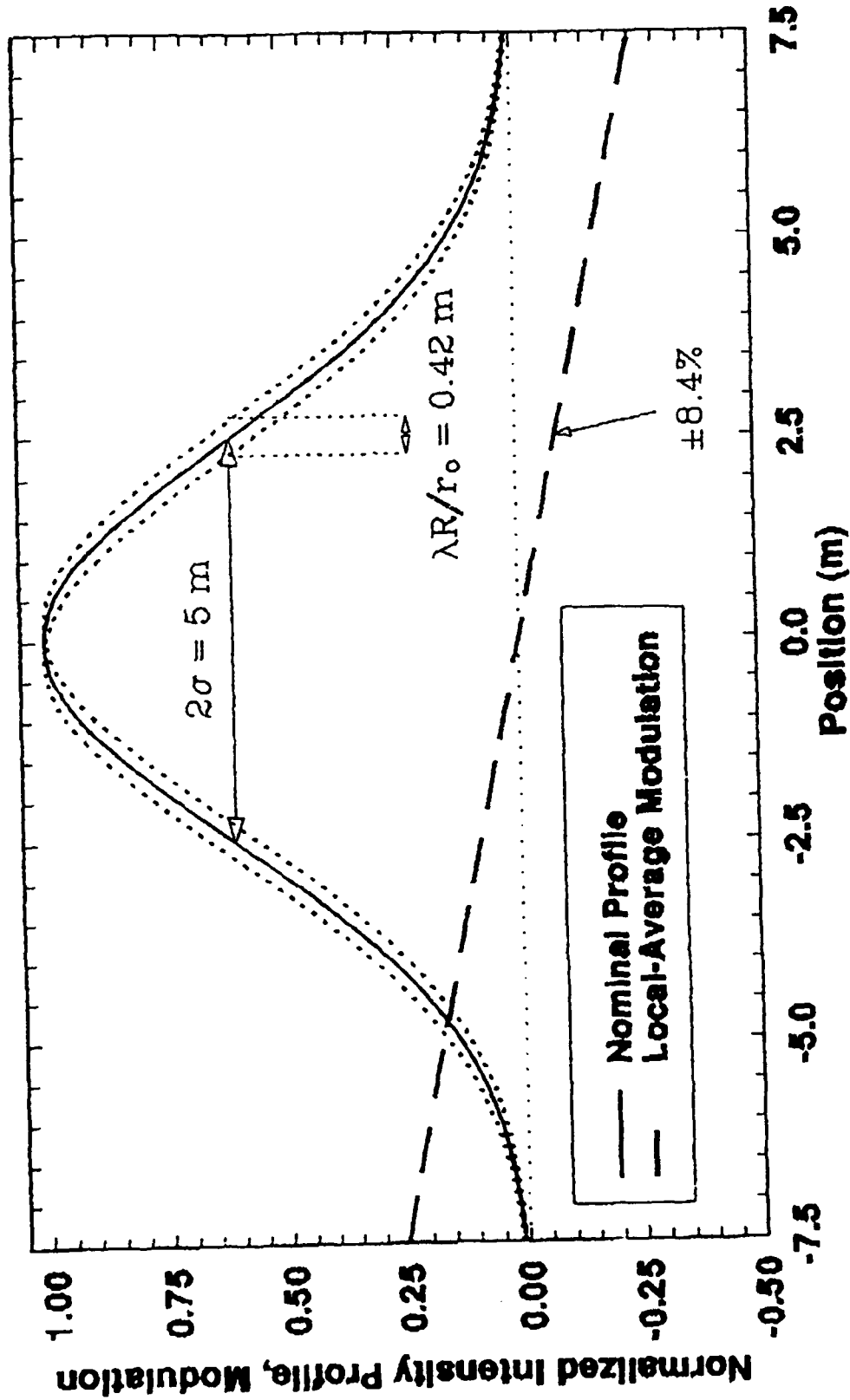


Table I.
TARGET & SYSTEM PARAMETERS

	EOS T. Shultz	CREOL P. Gatt	WJSA F. Tart
energy/pulse	0.8 J/8 nsec	0.8 J/8 nsec	0.5 J
τ_T	0.9	0.9	0.619
τ_R	0.25	0.25	0.486
τ_F	0.5	0.5	0.5
ρ , hard body	0.05/sr	$\rho \cos \theta / \pi$	$\rho / 2\pi$
ρ , plume	0.1/sr		0.1/sr
η	0.1	0.36	0.1
atm. transm.	0.5×0.5 (0.3 dB/km)	0.65 dB/km	0.5×0.5
pulse stretch	16 nsec	16 nsec	

Table II.
BACKGROUND

	EOS T. Shultz	CREOL P. Gatt	WJSA F. Tart
τ int. time	0.3 μ sec @ 0.532 0.8-1.6 W / cm ² sr μ m @ 1.06 16 W / cm ² sr μ m	60 MHz (16 nsec) T = 2300 K emissivity = 1	1 μ sec T = 2200 K emissivity = 0.2
FOV	$\Omega = 3.5 \times 10^{-9}$ sr	$\phi_{1/2} = 250 \mu$ rad (4.9 $\times 10^{-8}$ sr)	$\Omega = 1.661 \times 10^{-6}$ sr

APPENDIX: RADIOMETRIC CALCULATIONS

Figure A-1 defines the quantities employed in the radiometric analysis. A far-field formalism is employed, i.e., the laser beam is represented as subtending a transmission solid angle that is invariant with range, and likewise for the receiver viewing returns from the target. The fundamental quantity to be computed is the number of photoelectrons detected per resolution cell at the receiver, N_{res} ; this is done in two steps. One first computes the expected value for the total number of photoelectrons in the entire image (N_{total}); one then divides by the number of resolution elements (resels) to obtain N_{res} .

The total number of photoelectrons is represented in Figure A-1 as the product of four terms: (1) the number of photons transmitted by the laser to the vicinity of the target (including the outward-bound atmospheric loss factor); (2) the target reflection cross section; (3) the fraction of the scattered radiation which is collected by the receiver entrance pupil (including the return-trip atmospheric loss factor); and (4) the receiver photoelectron efficiency.

The dependence of the number of signal photoelectrons on atmospheric conditions is summarized in Figure A-2. The round-trip loss factor is assumed to be governed by the exponential (Beer-Bouguer) law shown--i.e., single scattering is assumed.

The number of resels in the image is assumed to be governed primarily by atmospheric turbulence. The limiting angular resolution θ_{atm} imposed by clear-air turbulence is determined by Fried's coherence diameter r_0 through the approximate relation, $\theta_{atm} = \lambda/r_0$.

It has been assumed that the principal source of noise arises from the radiance of the rocket plume. The plume is modeled as a greybody, i.e., a Planckian radiator with a specified emissivity and color temperature. As indicated in Figure A-3, the total number of background photons is again the product of four factors: (1) the number of photons emitted by the plume per unit area; (2) the observed target area (product of R^2 and the solid angle subtended by the receiver field of view); (3) the fraction intercepted by the receiver (including a *one-way* atmospheric loss factor); and (4) the receiver efficiency. Once again, to calculate the number of photoelectrons per pixel, one divides the receiver FOV by the number of turbulence-limited pixels which it spans.

Figure A-4 indicates the parameter values employed in the analysis.

RADIOMETRIC ANALYSIS

Entire Beam on Target

Transmitted photons	Target cross-section	Received fraction	Receiver photoelectron efficiency
---------------------	----------------------	-------------------	-----------------------------------

$$[(E/h\nu)\tau_t \tau_a] \times [\rho (\pi/4)R^2\Theta^2] \times [\tau_a (A_r/R^2)] \times [\tau_r \tau_f \eta] = N_{\text{total}}$$

Conversion to per-resel basis Photoelectrons per Resolution Cell

$$N_{\text{total}} \times [(\lambda/r_o)^2/\Omega_t] = N_{\text{res}}$$

where: E = Energy (Joules) per pulse, h = Planck constant (J/Hz),

ν = laser frequency (Hz), τ_t = transmitter efficiency,

τ_a = one-way atmospheric transmission,

ρ = effective reflectance (sr^{-1}), $\Theta = \min(\Theta_t, \Theta_r)$ (rad),

A_r = receiver aperture (m^2), R = slant range (m),

τ_r = receiver efficiency, τ_f = filter efficiency,

η = quantum efficiency, λ = wavelength (m),

N_{total} = Total number of photoelectrons received,

r_o = Fried's coherence diameter (m),

Ω_t = transmission solid angle (sr) = $\pi\Theta_t^2/4$, and

N_{res} = Number of photoelectrons per effective resolution cell.

Figure A-1. Radiometric analysis of signal photocounts per resel.

Figure A-2.

Atmospheric Parameters vs Slant Range (Under Uniform Conditions)

Transmission (2-way):

$$T_a^2 = \exp(-2\alpha R)$$

where α = attenuation coefficient (m^{-1}),
and R = slant range (m).

Turbulence (Coherence Diameter):

Fried's coherence diameter = r_o (m)

defined by Wave Structure Function $D_w(\rho)$:

$$D_w(\rho) = 6.88 (\rho/r_o)^{5/3}, \text{ where}$$

ρ = transverse separation across wavefront.

For plane waves, $k=2\pi/\lambda$, turbulence uniformly of strength

C_n^2 ($m^{-2/3}$) along the slant path:

$$r_o = (0.4233 C_n^2 k^2 R)^{-3/2}$$

Typically, r_o should be several centimeters.

$$N_{total} = \underbrace{\frac{\epsilon_{bkgd} P_{bb}(\lambda; T_c)}{h\nu}}_{\text{emitted photons/area}} \Delta t \Delta \lambda \times \underbrace{\Omega_{FOV} R^2}_{\text{obs. area}} \times \underbrace{\tau_A \frac{A_r}{R^2}}_{\text{rcvd. fraction}} \times \underbrace{\tau_r \tau_f \eta}_{\text{efficiency}}$$

$$N_{res} = N_{total} \times \frac{(\lambda/r_o)^2}{\Omega_{FOV}}$$

- Ω_{FOV} - $\pi\Theta_r^2/2$ (sr)
- ϵ_{bkgd} - effective greybody emissivity
- $P_{bb}(\lambda; T_c)$ - Planckian spectral radiance ($W m^{-2} \mu m^{-1} sr^{-1}$)
at wavelength λ (μm) and color temperature T_c (K)
- h - Planck constant
- Δt - receiver integration time (sec)
- $\Delta \lambda$ - receiver spectral bandwidth (μm)
- R - range (m)
- τ_A - 1-way atmospheric attenuation (range-dependent)
- A_r - receiver area (m^2)
- τ_r, τ_f - receiver and filter efficiencies
- η - quantum efficiency
- r_o - Fried's coherence diameter (m)

Figure A-3. Radiometric analysis of background photocounts per resel.

Figure A-4.

RADIOMETRIC ANALYSIS

Parameters Employed

for radiometric analysis.

Parameter	Value	Parameter	Value
E (J/pulse)	0.8	ϵ bkgd	0.78
$\lambda(\mu\text{m})$	0.532	$T_c(\text{K})$	2230
τ_t	0.9	$\Theta_r(\mu\text{rad})$	300 (Case 1) 600 (Case 2)
τ_a (one way)	$0.5^{R/10}$ km	$\Delta t(\mu\text{sec})$	0.4
ρ_{plume} (sr^{-1})	0.1	$\Delta\lambda(\mu\text{m})$	0.001
ρ_{hardbody} (sr^{-1})	0.05		
R(km)	10 to 30		
$\Omega_t(\text{sr})$	4.0×10^{-8} (Case 1) 2.5×10^{-7} (Case 2)		
$\Omega_r(\text{sr})$	7.0×10^{-8} (Case 1) 2.8×10^{-7} (Case 2)		
$A_t(\text{m}^2)$	0.5		
Beam-Splitting Ratio	$\approx 50:50$		
τ_r	0.5		
τ_f	0.9		
η (electrons/photon)	0.1		
$r_o(\text{m})$	0.05		